Functionalized biomimetic nanoparticles loaded with salvianolic acid B for synergistic targeted triple-negative breast cancer treatment

Nuo Cheng [a,b,1], Qianqian Zhou [a,b,1], Zongfang Jia [a,b,1], Yang Mu [a,b], Sheng Zhang [a,**], Lei Wang [a,b,c,***], Yunna Chen [a,*]

[a] Anhui University of Chinese Medicine, Hefei, 230012, China
[b] MOE-Anhui Joint Collaborative Innovation Center for Quality Improvement of Anhui Genuine Chinese Medicinal Materials, Hefei, 230012, China
[c] Institute of Pharmaceutics, Anhui Academy of Chinese Medicine Key Laboratory of Pharmaceutical Preparation Technology and Application, Hefei, 230012, China

ARTICLE INFO

ABSTRACT

The therapeutic effect of immune checkpoint inhibitors (ICIs) in triple-negative breast cancer (TNBC) is unsatisfactory. The immune "cold" microenvironment caused by tumor-associated fibroblasts (TAFs) has an adverse effect on the antitumor response. Therefore, in this study, mixed cell membrane-coated porous magnetic nanoparticles (PMNPs) were constructed to deliver salvianolic acid B (SAB) to induce an antitumor immune response, facilitating the transition from a "cold" to a "hot" tumor and ultimately enhancing the therapeutic efficacy of immune checkpoint inhibitors. PMNP-SAB, which is based on a mixed coating of red blood cell membrane and TAF membrane (named PMNP-SAB@RTM), can simultaneously achieve the dual effects of "immune escape" and "homologous targeting". Under the influence of an external magnetic field (MF), SAB can be targeted and concentrated at the tumor site. The SAB released in tumors can effectively inhibit the production of extracellular matrix (ECM) by TAFs, promote T-cell infiltration, and induce antitumor immune responses. Ultimately, the combination of PMNP-SAB@RTM and BMS-1 (PD-1/PD-L1 inhibitor 1) effectively inhibited tumor growth. Finally, this study presents a precise and effective new strategy for TNBC immunotherapy on the basis of the differentiation of "cold" and "hot" microenvironments.

1. Introduction

Triple-negative breast cancer (TNBC) is the most aggressive subtype of breast cancer. It is characterized by the absence of estrogen receptor (ER) and progesterone receptor (PR) expression, as well as the absence of amplification or overexpression of human epidermal growth factor receptor 2 (HER2) [1,2]. Early relapse and the absence of therapeutic targets are significant challenges in the treatment of TNBC [3,4]. Owing to the large number of tumor-infiltrating lymphocytes (TILs) and high expression of PD-L1, immunotherapy is considered a breakthrough in the clinical treatment of TNBC [5]. However, only a small number of patients can benefit from immunotherapy, and the treatment effect is not ideal for most patients [6,7]. The widespread application of immunotherapy still faces many challenges in the future [8]. The tumor microenvironment (TME) has a significant effect on immunotherapy

[9–12]. TNBC can be divided into three heterogeneous clusters on the basis of its microenvironmental phenotype [13]. Cluster 1, a type of microenvironment with low cell infiltration, is known as the "immune desert" cluster. Cluster 2 contains partially dormant infiltrating innate immune cells and nonimmune stromal cells and is known as the "innate immune-inactivated" cluster. Cluster 3 is an "immune inflamed" cluster characterized by the significant presence of many adaptive and innate cells infiltrating the area. Among them, the "immune desert" cluster and the "immune inflamed" cluster microenvironments are considered "cold" tumors, and immunotherapy has no significant therapeutic effect on them [14]. Therefore, transforming "cold" tumors into "hot" tumors is a strategy to increase the effectiveness of immune checkpoint inhibitors (ICIs) [15].

Tumor-associated fibroblasts (TAFs) are key cellular components in the tumor stroma that promote tumor growth [16,17]. TAFs are situated

primarily at the periphery of infiltrated tumors, converting the tumor edge into an immunologically "cold" zone through the synthesis and remodeling of the extracellular matrix (ECM) and the production of cytokines [18,19]. This process regulates tumor metastasis and impacts angiogenesis. TAFs induce immunosuppression and T-cell rejection through various mechanisms. First, the ECM produced by TAFs forms a physical barrier to prevent T cells from infiltrating into the tumor area [20]. Second, CXCL12 produced by TAFs has been shown to inhibit T lymphocyte infiltration within tumors [21]. Third, TAFs can reduce T-cell responses and exert immunosuppressive effects through the production of transforming growth factor-β (TGF-β) and IL-6 [22,23]. TGF-β is a potent immunosuppressive cytokine that promotes immune evasion and inhibits the development of the TH1 effector phenotype [24]. TAFs, which are abundant in the TME, are the main producers of TGF-β [25]. TGF-β restricts the proliferation of CD4$^+$ T lymphocytes and induces the transformation of CD4$^+$ T lymphocytes into Tregs by inhibiting IL-2 production [26]. TGF-β also interferes with T-cell initiation by negatively affecting dendritic cell (DC) differentiation and antigen-presenting functions [27]. In summary, TAFs hinder antitumor immunity by generating ECM and TGF-β, which impact T-cell differentiation and function and hinder T-cell infiltration into the tumor. Therefore, inhibiting TAFs is an effective strategy to transform tumors from being immune "cold" to being immune "hot" and enhancing TNBC immunotherapy.

Salvianolic acid B (SAB) is the water-soluble component with the highest content extracted from the traditional Chinese medicine Danshen. Research has shown that SAB has antifibrotic and collagen-generating effects [28,29]. Our previous research also revealed that SAB can inhibit the activation of TAFs and reduce ECM deposition [30]. Although studies have reported that SAB does not affect breast tumor growth, it can inhibit tumor metastasis and enhance the therapeutic effect of ICIs [31]. However, the active ingredients of traditional Chinese medicine have the disadvantages of a short half-life and poor targeting, leading to inadequate drug enrichment at the lesion site and a limited therapeutic effect [32]. In recent years, research on nanodelivery systems has played a crucial role in increasing the efficacy of active ingredients in traditional Chinese medicine [33,34]. In addition, nanotechnology has great potential in enhancing the immune response of cancer patients [35–38]. Although there have been studies using nanoparticles to deliver SAB to tumors, the lack of targeting makes it difficult to accurately deliver SAB to TAFs [30]. Porous magnetic nanoparticles (PMNPs) are the first nanomaterials approved by the U.S. Food and Drug Administration for clinical use. They offer unique advantages in magnetic resonance imaging, magnetic targeted drug delivery, and hyperthermia applications [39]. When PMNPs are utilized as drug carriers, they can passively target drug delivery by applying an enhanced magnetic field (MF) at the lesion site [40]. In addition, PMNPs can also increase the temperature of pathogenic sites through near-infrared light irradiation, thereby accomplishing the objective of thermotherapy [41]. However, PMNPs are easily cleared by the immune system when administered *in vivo* and cannot target specific cells. Therefore, developing low-immunogenicity targeted PMNPs has become a research hotspot. The modification of nanocarrier systems by extracting and isolating cell membranes from biological cells can help achieve the objectives of immune evasion and homologous targeting [42,43]. CD47 is a surface protein found on the red blood cell membrane (RBCM) that can emit a "do not eat me" signal in certain regions, thus suppressing the phagocytic activity of macrophages [44]. In addition, cell membranes derived from pathogenic tissues typically exhibit homologous targeting characteristics and can be modified on the surface of nanoparticles to deliver drugs to pathogenic sites [45]. Therefore, the mixed modification of RBCM and TAF membranes (TAFM) on the surface of PMNPs can not only evade immune system clearance but also "self-recognize" and accurately target TAFs, providing conditions for efficient targeted delivery of SAB.

In this study, the multifunctional biomimetic nanoparticles loaded with SAB were developed to treat TNBC (Scheme 1). This nanoparticle enhanced T-cell infiltration by inhibiting TAF activation, promoted the transformation of "cold" tumors into "hot" tumors, and consequently enhances the sensitivity of ICIs. SAB was embedded in the PMNPs, and then the extracted RBCM and TAFM were coated onto the surface of the PMNP-SAB to successfully construct multifunctional biomimetic nanoparticles (PMNP-SAB@RTM). After entering the body, PMNP-SAB@RTM were disguised by RBCM, which could successfully prolong their circulation time in the bloodstream. On the other hand, PMNP-SAB encapsulated by the TAFM have membrane antigens and the structures of TAFs, enabling specific targeting of TAFs. In addition, under the influence of external MF, more PMNP-SAB@RTM accumulated at the tumor site. PMNP-SAB@RTM targeted TAFs homologously and released SAB to inhibit TAF activity, thereby reducing ECM deposition. The infiltration of immune cells into tumors subsequently increased, leading to the transformation of "cold" tumors into "hot" tumors and enhancing the antitumor immune response. Moreover, the therapeutic sensitivity of ICIs (BMS-1) was enhanced, inhibiting tumor growth and improving the immunotherapeutic effect on TNBC. This strategy of transforming "cold" tumors into "hot" tumors opens up new avenues for immunotherapy.

2. Methods

2.1. Materials

SAB (purity: 99.39 %) was purchased from Chengdu Pufei De Biotech Co., Ltd. Iron (III) trichloride hexahydrate (FeCl$_3$-6H$_2$O) was purchased from Shanghai Aladdin Biochemical Technology Co., Ltd. Ferrous chloride (FeCl$_2$-4H$_2$O) was provided by Tianjin Guangfu Technology Development Co., Ltd. Cetyltrimethylammonium bromide (CTAB, content≥99 %) was purchased from Shanghai Yuanye Bio-Technology Co., Ltd. Ammonium hydroxide was acquired from Sinopharm Chemical Reagent Co., Ltd. Hydrochloric acid (content: 36.0 %–38.0 %) was purchased from Chengdu Cologne Chemical Co., Ltd. DMEM was purchased from Shandong Sparkjade Biotechnology Co., Ltd. Fetal bovine serum was purchased from Thermo Fisher Scientific. Penicillin–streptomycin was acquired from Beyotime Biotechnology. Human TGF-β1 was obtained from Shenzhen Xinbosheng Biotechnology Co., Ltd. DiL (cell membrane red fluorescent probe) and DiO (cell membrane green fluorescent probe) were purchased from Dalian Boglin Biotechnology Co., Ltd. Anti-CD45, anti-CD3, anti-CD4, anti-CD8, anti-F4/80, anti-CD86, anti-CD206, anti-CD25, and anti-Foxp3 antibodies were purchased from Elabsceince.

2.2. Cell culture

Mouse breast cancer 4T1 cells and mouse embryonic fibroblasts (NIH3T3) were obtained from HAKATA Biotechnology Co., Ltd. RAW264.7 cells were acquired from the Cell Bank for Type Culture Collection of the Chinese Academy of Science. NIH3T3 and RAW264.7 cells were cultured in DMEM containing 10 % FBS and 1 % penicillin streptomycin. 4T1 cells were cultured in RPMI medium supplemented with 10 % FBS and 1 % penicillin streptomycin. All the samples were maintained at 37 °C in a humidified environment containing 5 % CO$_2$.

2.3. Animals

Female BALB/c mice were purchased from the Experimental Animal Center of Anhui Medical University. All animal experiments were approved by the Animal Management and Use Committee of Anhui University of Traditional Chinese Medicine (AHUCM-mouse-2023170).

2.4. Synthesis of PMNP-SAB

The preparation of the PMNPs followed a previously described
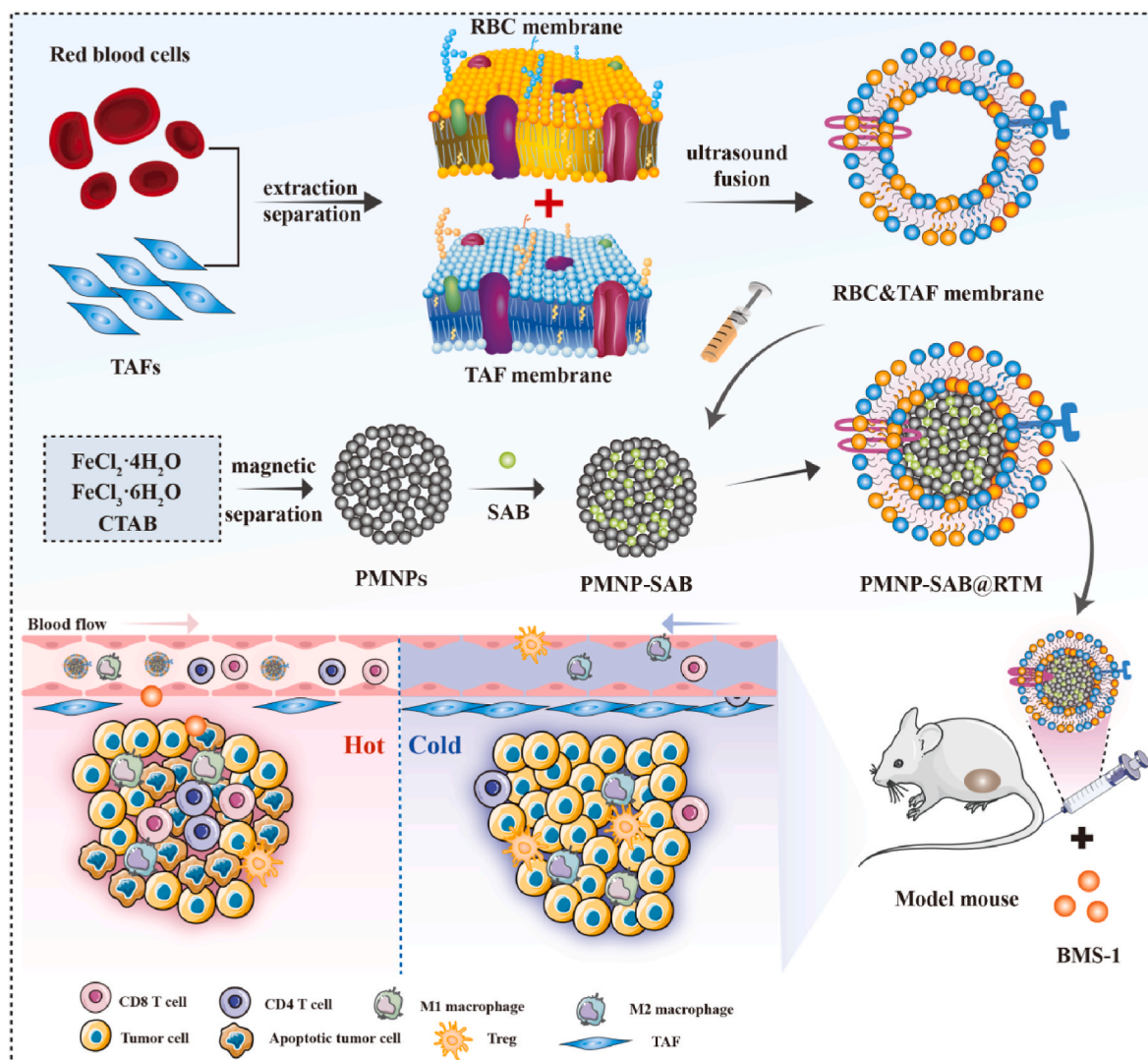
Scheme 1. Schematic illustration of the preparation and tumor immunotherapy of PMNP-SAB@RTM. PMNP-SAB@RTM were prepared by modifying isolated RBCM and TAFM on PMNP-SAB. PMNP-SAB@RTM promoted the transformation of "cold" tumors into "hot" tumors, enhancing the antitumor efficiency of BMS-1.

method [46]. $FeCl_2 \cdot 4H_2O$ (0.5 g), $FeCl_3 \cdot 6H_2O$ (1 g), and CTAB (300 mg) were thoroughly mixed in 25 mL of ultrapure water. Then, 25 mL of ammonium hydroxide (NH_3-H_2O, 33 %) was added dropwise with vigorous stirring. After 2 h, the product was separated via a permanent magnet and washed three times with ethanol. The product was incubated in a solution containing hydrochloric acid (HCl, 0.6 % v/v) and methanol for 1 h to remove the CTAB template. The mixture was separated via a magnetic field and washed with ethanol to obtain PMNPs. The PMNPs were freeze-dried and stored at room temperature for future use.

To obtain PMNPs wrapped in SAB, an appropriate amount of PMNPs or SAB was mixed in ultrapure water and incubated at room temperature for 6 h. After centrifugation, the precipitate was washed with ultrapure water to obtain PMNP-SAB, and all the supernatants obtained during the centrifugation process were collected. The content of SAB in the supernatant was analyzed via HPLC (detection wavelength: 286 nm) to determine the drug loading of PMNP-SAB.

2.5. Preparation of RBCM

Whole blood was collected from 7-week-old female BALB/c mice and centrifuged at 4 °C (2000 rpm) for 10 min to separate the plasma. Then, precooled 1 × PBS buffer was added to the precipitate, the mixture was centrifuged at 3000 rpm for 10 min, and the supernatant was discarded. This step was repeated three times to obtain RBCs. RBCs were mixed at a volume ratio of 1:10 in 0.25 × PBS buffer and left at 4 °C for 1 h to promote hemolysis. After incubation, the mixture was centrifuged at 12000 rpm for 10 min to remove hemoglobin. Next, the precipitate was washed repeatedly with 0.25 × PBS until the supernatant was almost colorless, resulting in a pink precipitate called RBCM. The RBCM was stored at −20 °C and thawed at 4 °C before use.

2.6. Acquisition of the TAFM

Before TAFM was extracted, the NIH3T3 cells were treated with TGF-β1 (10 ng/mL) for 24 h to obtain TAFs. Then, the TAFs were collected, and a lysis solution containing 1 % PMSF was added. An ultrasonic cell crusher (150 W, 10 min) was used for sufficient cell lysis. The cell lysate was centrifuged (3200×g) at 4 °C for 5 min to remove intact cells and nuclei. Next, the supernatant was centrifuged (20000×g) at 4 °C for 20 min to remove cell debris. Finally, the collected supernatant was centrifuged (100000×g) at 4 °C for 45 min, and the precipitate was removed to obtain the TAFM. TAFM was stored at −20 °C and thawed at 4 °C before use.

2.7. Preparation of PMNP-SAB@RTM

RBCM and TAFM were mixed with equal amounts of membrane proteins and then fused via an ultrasonic cell lysis machine (150 W, 10 min) to obtain a mixed membrane ([RBC&TAF]m). The extrusion method was used to prepare PMNP-SAB@RTM. The fusion membrane prepared previously was thoroughly mixed with the PMNP-SAB suspension. The mixture was then extruded multiple times through 400 nm and 200 nm polycarbonate membranes to obtain PMNP-SAB@RTM. The product was refrigerated at 4 °C for future use.

2.8. Characterization

The PMNP, PMNP-SAB, and PMNP-SAB@RTM samples were thoroughly sonicated in ultrapure water and then diluted to an appropriate concentration. The particle size, dispersion index, and zeta potential values of the samples were measured via a Zetasizer (Malvern Instruments Ltd., UK). Transmission electron microscopy (TEM) was used to observe the morphology of the PMNPs, PMNP-SAB, and PMNP-SAB@RTM. A vibration sample magnetometer was used to measure the magnetic strength of the PMNPs and PMNP-SAB@RTM. To verify the successful fusion of the RBCM and TAFM, DiO and DiL were selected to label the TAFM. Foster resonance energy transfer (FRET) was utilized to detect changes in fluorescence intensity following the gradual addition of RBCM to TAFM. In addition, to observe the fusion of RBCM and TAFM more directly, DiO-labeled TAFM and DiL-labeled RBCM were mixed together at a 1:1 ratio on the basis of protein weight. After 10 min of ultrasonication, the fusion protein was observed under a fluorescence inverted microscope. The N_2 adsorption/desorption isotherm technique was used to determine the specific surface area and pore structure of PMNPs and SAB-PMNP. The coomassie brilliant blue gel staining method was used to analyze the changes in surface protein content after RBCM and TAFM were subjected to hypotonic lysis, extrusion, and other steps. Western blot was used to detect the expression of key proteins CD47, AE1, and FAP1 on PMNP-SAB@RTM. Changes in the particle size and potential values of the PMNPs, PMNP-SAB, and PMNP-SAB@RTM were observed within one week to evaluate the stability of the formulation. One milliliter each of the SAB and PMNP-SAB@RTM solutions was placed in a dialysis bag to investigate the release efficiency in a PBS solution (pH 7.4).

2.9. In vitro cytotoxicity assay

$$\text{Hemolysis rate} = \left(\text{OD}_{\text{Sample group}} - \text{OD}_{\text{Negative control group}}\right) / \left(\text{OD}_{\text{Positive control group}} - \text{OD}_{\text{Negative control group}}\right) \times 100\%$$

CCK8 and Annexin-V/PI assay kits were used to determine cell survival rate. Specifically, TAFs were seeded in a 96-well plate (5×10^3 cells/well). After 12 h of cultivation, the supernatant was removed and different concentrations of nanoparticles were added to a 96-well plate. After 24 h, 100 μL of CCK-8 solution was added to each well and incubated at 37 °C for 30 min. Finally, the microplate reader was used to measure cell viability. Flow cytometry was used to detect cell apoptosis. After treating 4T1 cells with different nanoparticles (SAB:100 μM) and BMS-1 (25 μM) for 24 h, the Annexin-V/PI kit was used to detect cell apoptosis.

2.10. Homologous targeting and immune escape ability

4T1, TAF, and NIH3T3 cells were used to evaluate the targeting capability of PMNP-SAB@RTM. First, 4T1, TAF, and NIH3T3 cells were cultured in 6-well plates for 24 h. Then, the DiL-labeled biomimetic nanosuspension (DiL-PMNP-SAB@RTM, with 100 μg/mL PMNPs) was added to the cells for 3 h. The cells were washed with precooled PBS (pH 7.4) to remove residual agents, and the nuclei were stained with Hoechst 33258 for 20 min. Finally, confocal laser microscopy (FV3000, OLYMPUS) was used to observe the uptake of the nanoparticles by the 4T1, TAF, and NIH3T3 cells. Flow cytometry was used to measure the uptake of the nanoparticles by the 4T1, TAF, and NIH3T3 cells quantitatively. RAW264.7 cells were used to investigate the immune evasion capability of DiL-PMNP-SAB@RTM. After 1 h of nanoparticles treatment, the cells were processed as described above to assess macrophage phagocytosis of the nanoparticles.

2.11. Fluorescence imaging in vivo

4T1 cells were subcutaneously injected into the fourth pair of breast pads (1×10^6) of BalB/c female mice to establish a tumor-bearing mouse model. DIR dyes were used to replace the SAB loaded into the nanoparticles to prepare PMNP-DIR@RTM. DIR, PMNP-DIR and PMNP-DIR@RTM (DIR: 2 mg/kg) were injected into the tail vein of the model mice, and plasma was collected for imaging at specific time points. The IVIS Spectrum imaging system was used to observe the distribution of nanoparticles at different time points while the subjects were under anesthesia. After 24 h of nanoparticle treatment, the tumors and major organs of the mice were removed for in vitro imaging. In addition, we further observed the effect of an external MF on the distribution of the nanoparticles in vivo. Free SAB and PMNP-SAB@RTM (SAB: 20 mg/kg) were injected into the tail vein of SD rats to study their in vivo behavior. Ultra high performance liquid chromatography was used to determine the concentration of SAB in plasma at different time points.

2.12. Hemolysis test of PMNP-SAB@RTM

Healthy rabbit heart blood was collected to prepare a 2 % red blood cell suspension. A series of different concentrations of SAB and PMNP-SAB@RTM were mixed with an equal volume of 2 % red blood cell suspension. A 0.9 % sodium chloride solution was used as a negative control, whereas deionized water was used as a positive control. All the samples were imaged after incubation at 37 °C for 3 h. The absorbance of the supernatant at 540 nm was measured. The hemolysis rate was calculated as follows:

2.13. Antitumor effects in vivo

Female BALB/c mice were used to establish an in situ TNBC model. When the tumor volume increased to approximately 50 mm³, the tumor-bearing mice were randomly divided into five groups (six in each group), namely the model group, the BMS-1 group, the PMNP-SAB@RTM group, the BMS-1+PMNP-SAB@RTM group, and the BMS-1+PMNP-SAB@RTM + MF group. The mice in the BMS-1 group were then intraperitoneally injected with BMS-1 (6 mg/kg) every other day. The mice in the PMNP-SAB@RTM group were injected with PMNP-SAB@RTM (SAB: 20 mg/kg) via the tail vein every other day. The mice in the BMS-1+PMNP-SAB@RTM group were administered a combination of substances on the basis of their respective administration methods. The mice in the BMS-1+PMNP-SAB@RTM + MF group were treated with an external MF. After drug injection, the magnet block was

fixed at the tumor site of the mouse to apply an external MF [47]. In addition, the mice in the control group were injected with physiological saline. Changes in tumor volume and mouse weight trends were observed throughout the entire experimental process. The formula for calculating tumor volume was as follows: tumor volume $(mm^3) = 0.5 \times length \times width^2$. After the experiment, the tumors were collected for weighing and photography. The survival time of tumor bearing mice was recorded. Mice with unilateral tumors exceeding 15 cm in length were considered dead. Serum and major organs are used to evaluate the safety of formulations. The ELISA kits were used to measure the levels of CXCL9, CXCL10, CXCL12, IFN-γ, TNF-α and IL-6 in tumors.

2.14. Western blot analysis

The removed tumor tissues were collected and lysed with RIPA buffer to extract total protein. A BCA protein assay kit was used to determine the protein concentration. Sodium dodecyl sulfate polyacrylamide gel electropheresis (SDS–PAGE, 10 %) was used to separate each sample, which was subsequently transferred onto a PVDF membrane. At room temperature, the membrane was blocked in 5 % skim milk for 2 h and then incubated with an α-SMA primary antibody. On the second day, the membrane and secondary antibody were incubated at room temperature for 2 h before the protein signals were detected via an enhanced chemiluminescence system.

2.15. Masson's trichrome staining

The removed tumor tissue was collected for paraffin embedding and sectioning, stained with a Masson staining kit, and finally, Masson's trichrome staining of the tumor sections was performed via a microscope. The images were quantitatively analyzed via Image J software. To investigate whether the inhibition of TAFs by PMNP-SAB@RTM could reduce ECM deposition in tumor tissues and eliminate the physical barrier to T-cell infiltration.

2.16. TUNEL assay

The collected tumor tissue was fixed in 4 % paraformaldehyde and dehydrated in 20 % sucrose solution. Afterward, the tissue was cut into frozen sections of approximately 25 μm. Slices were stained via a reagent kit as instructed. Finally, the THUNDER imaging system (Leica, DMi8) was used to capture images. ImageJ software was used to analyze the process of cell apoptosis.

2.17. Flow cytometry analysis

To analyze the recruitment of immune cells in tumor tissue, fresh tumor tissues were collected for flow cytometry analysis. First, the tumor tissue was digested with collagenase IV and hyaluronidase at 37 °C for 1 h to form a single-cell suspension. The cell concentration was adjusted to 1×10^7 cells/mL. Next, CD16/CD32 antibodies were used to block cell suspensions and reduce nonspecific antibody binding. Antibodies are selected on the basis of the specific surface markers of immune cells and are stained according to the manufacturer's instructions. Finally, flow cytometry (BD FACSCelesta) was used for analysis.

2.18. Safety assessment

H&E staining was used to observe the pathological conditions of major organs in the mice in the various treatment groups. According to the kit instructions, changes in the serum levels of the liver and kidney function indices CK, ALT, AST, CRE, and BUN were detected in each group after administration.

2.19. Statistical analysis

All the experimental data are presented as the mean ± SD. GraphPad Prism 8.0 software and SPSS Statistics 21 were used for one-way ANOVA and two-tailed Student's *t*-test analysis. $p < 0.05$ was considered statistically significant.

3. Results

3.1. Preparation and characterization of PMNP-SAB@RTM

Before preparing PMNP-SAB@RTM, we extracted and isolated TAFM and RBCM. Then, the TAFM and RBCM were mixed and encapsulated on the surface of the magnetic nanoparticles (Scheme 1). To verify the successful fusion of the TAFM and RBCM, DiO and DiL were used to label the TAFM. RBCM was then gradually added to DiO and DiL double-labeled TAFM, and fusion was observed via Förster resonance energy transfer (FRET) [48–50]. The results are shown in Fig. 1A, where the fluorescence intensity decreased with increasing RBCM at 520 nm. The reason for this phenomenon is that the addition of RBCM changed the distance between DiO and DiL. This result implies that the RBCM was successfully inserted into the TAFM. In addition, to directly observe the hybridization of RBCM and TAFM, DiO-labeled TAFM and DiL-labeled RBCM were mixed together at a 1:1 protein weight ratio. Fluorescence microscopy was conducted to observe the colocalization of the two cell membranes after sonication and mixing at 37 °C for 10 min. Compared with those of the TAFM and RBCM mixtures, the fluorescent spots of TAFM (green) and RBCM (red) were significantly clustered after sonication incubation (Fig. 1B). In addition, the fluorescence curves of DiO and DiL overlapped after sonication incubation, whereas this phenomenon did not occur for the mixtures (Fig. 1C). These results further demonstrate that TAFsM and RBCM were successfully hybridized.

After TAFM and RBCM were successfully fused, SAB-loaded PMNPs were prepared. Next, PMNP-SAB@RTM was prepared by hybridizing a film mixed with magnetic nanoparticles and then repeatedly extruded. TEM was used to observe the morphology of the different nanoparticles. As shown in Fig. 1D, the PMNPs were porous spherical structures formed by the adsorption and aggregation of numerous small particles into clusters. The nanoparticle morphology was not significantly altered after SAB was encapsulated. After PMNP-SAB@RTM was coated with the hybrid film, a distinct film structure was visible on the surface, indicating successful coating of the nanoparticle surface. A Zetasizer was used to determine the size of the nanoparticles. The results are shown in Fig. 1E. The diameters of the PMNPs, PMNP-SAB, and PMNP-SAB@RTM were (175.3 ± 2.10) nm, (175.5 ± 1.06) nm, and (184.6 ± 0.70) nm, respectively. Among them, the diameter of PMNP-SAB@RTM increased by ~9 nm compared with that of PMNP-SAB, which is roughly the same as the thickness of cell membranes reported in the literature. This finding indicates that the hybrid cell membrane is likely to successfully cover the surface of the nanoparticles. The PDI values of PMNPs, PMNP-SAB, and PMNP-SAB@RTM were (0.122 ± 0.016), (0.100 ± 0.027), and (0.135 ± 0.021), respectively. The PDI values of the different formulations were less than 0.3, indicating a uniform size distribution of the nanoparticles. The results in Fig. 1F show that the zeta potential value of the PMNPs was -30.0 ± 2.05 mV. After loading the negatively charged drug SAB, the zeta potential decreased to -42.4 ± 4.47 mV. The zeta potential of PMNP-SAB@RTM was finally -35.1 ± 2.50 mV after the hybrid film coating. The maximum encapsulation rate (approximately 97.28 %) of PMNP-SAB was achieved when the mass ratio of PMNPs to SAB was 2:1. The drug-loading of PMNP-SAB at this point was ~33.19 %. N_2 adsorption/desorption was used to verify the mesoporous structure of PMNPs. As shown in Fig. 1G, the BET surface area of PMNPs was 116.97 m^2/g. The pore volume was 0.13 cm^3/g, and the most probable pore size was 4.34 nm. These results indicated that PMNPs have a mesoporous structure. After loading SAB, the BET surface area (69.96 m^2/g), pore volume (0.06 cm^3/g) and pore size (3.66 nm) of the PMNP-
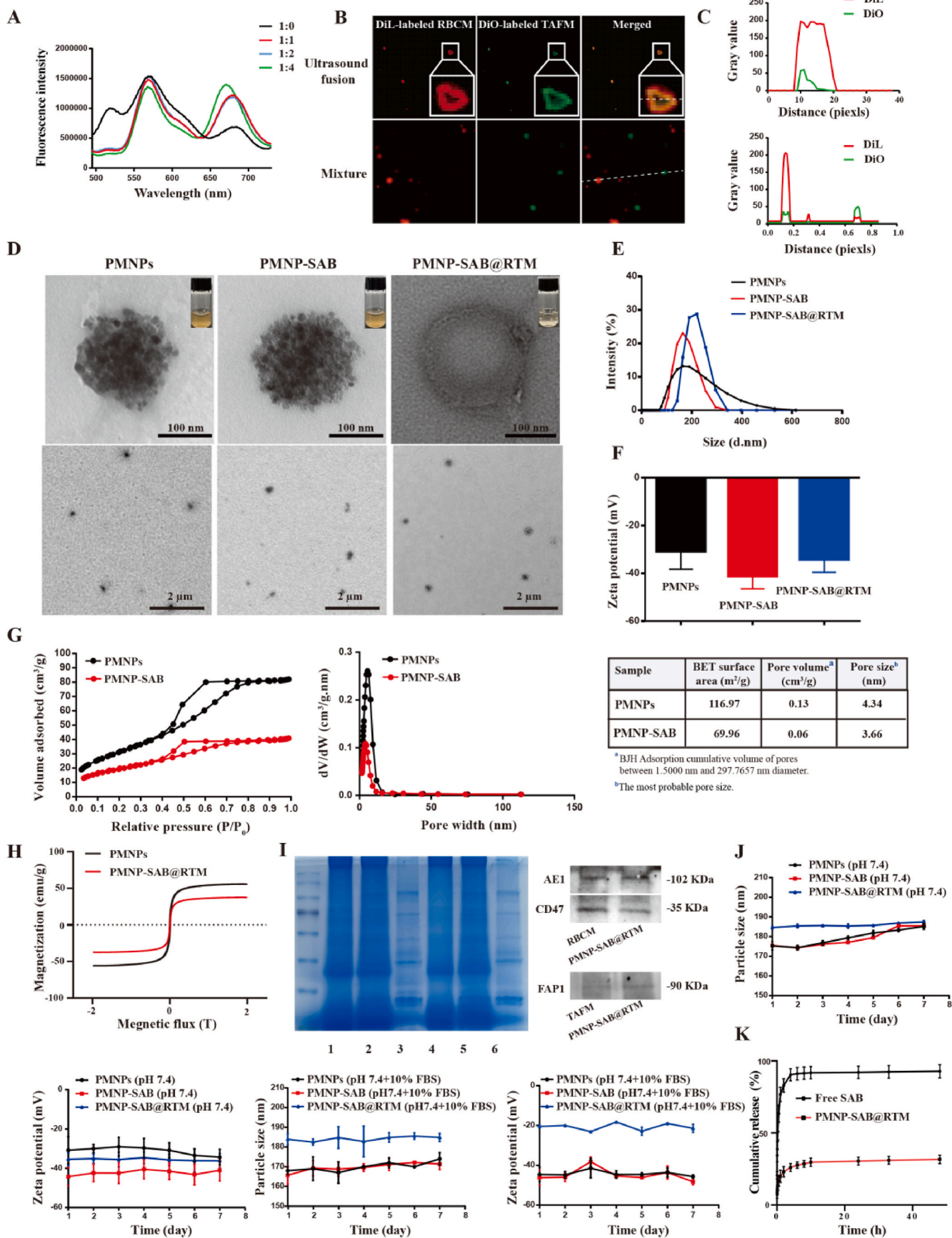
(caption on next page)

Fig. 1. Preparation and characterization of PMNP-SAB@RTM. (A) RBCM was added to DiO and DiL double-labeled TAFM and fusion was assayed via Förster resonance energy transfer. (B) Fluorescence images of the mixture of TAFsM and RBCM and the fusion membrane. (C) DiO and DiL fluorescence overlap curves. (D) TEM images of PMNPs, PMNP-SAB and PMNP-SAB@RTM. (E) Particle sizes of different formulations. (F) Zeta potentials of different formulations. (G) BET surface area and pore size distribution from BJH adsorption of PMNPs and PMNP-SAB. (H) Magnetization curves of the PMNPs and PMNP-SAB@RTM. (I) Protein bands were analyzed via SDS−PAGE. 1: RBCM, 2: RTM, 3: TAFM, 4: PMNP-SAB@RBCM, 5: PMNP-SAB@RTM, 6: PMNP-SAB@TAFM. Western blot analysis of the expression of AE1, CD47, and FAP1 on RBCM, TAFM and PMNP-SAB@RBCM. (J) Particle size and zeta potential variation curves of different formulations in pH 7.4 solution and pH 7.4 solution containing 10 % FBS. (K) The release behavior of SAB and PMNP-SAB@RTM.

SAB significantly decreased. This phenomenon indicated that SAB was successfully loaded into the PMNPs and occupied the mesoporous channels of the PMNPs. In addition, we observed excellent superparamagnetic properties of the PMNPs and PMNP-SAB@RTM. The saturation magnetization of the PMNPs was 55.8 emu/g, whereas that of the PMNP-SAB@RTM was 37.5 emu/g (Fig. 1H). The reason for the decrease in saturation magnetization of PMNP-SAB@RTM is the reduction in the PMNP content [51]. SDS−PAGE was performed to analyze whether PMNP-SAB@RTM successfully retained the protein bands of TAFM and RBCM during preparation. The results are shown in Fig. 1I, where many protein bands of PMNP-SAB@RTM were consistent with those of TAFM and RBCM, indicating that PMNP-SAB@RTM successfully retained the protein bands of TAFM and RBCM. The PMNP-SAB@RTM exhibited expression of CD47, AE1 (RBCM marker), and FAP1 (TAFM marker), indicating that the PMNP-SAB@RTM can possess both RBCM and TAFM characteristics simultaneously (Fig. 1I). We evaluated the placement stability of the PMNP-SAB@RTM in PBS solution or PBS solution containing 10 % FBS. There was no significant change in the particle size or potential of the different formulations after one week at 4 °C, indicating a certain level of stability (Fig. 1J). The significant decrease in the potential of PMNPs in 10 % FBS compared to those without 10 % FBS may be due to the formation of protein corona on the surface of PMNPs. Finally, the release behavior of free SAB and PMNP-SAB@RTM showed that all curves rose rapidly in the initial phase and eventually leveled off. Free SAB was cumulatively released by 90.40 % within 4 h, whereas only 29.69 % of the SAB was released from PMNP-SAB@RTM within 10 h (Fig. 1K). This result suggests that PMNP-SAB@RTM exhibited a slow release effect.

3.2. Immune escape, homologous targeting, and inhibition of TAFs by PMNP-SAB@RTM

After being encapsulated by a mixed membrane of RBCs and TAFs, the nanoparticles have dual functions of immune escape and homologous targeting (Fig. 2A). To determine whether the designed PMNP-SAB@RTM has the ability to evade phagocytosis by macrophages, various DiL-labeled preparations (PMNP-SAB@TAFM, PMNP-SAB@RBCM, and PMNP-SAB@RTM) were coincubated with RAW264.7 cells for 1 h. Phagocytosis by macrophages was observed via laser confocal microscopy. As shown in Fig. 2B, the red fluorescence of PMNP-SAB and PMNP-SAB@TAFsM aggregated within the RAW264.7 cells, whereas the red fluorescence shifted away from the RAW264.7 cells following PMNP-SAB@RBCM or PMNP-SAB@RTM treatment. The fluorescence profile of DiL-labeled PMNP-SAB and PMNP-SAB@TAFM overlapped with that of the Hoechst-labeled RAW264.7 cells. In contrast, the fluorescence curves representing PMNP-SAB@RTM and PMNP-SAB@RBCM overlapped less with those of RAW264.7 cells. These results suggest that RBCM or hybrid membrane-coated nanoparticles can evade phagocytosis by macrophages. Phagocytosis of the nanoparticles by the macrophages was further quantified via flow cytometry. Compared with that of PMNP-SAB-treated RAW264.7 cells, the average fluorescence intensity of PMNP-SAB@TAFM-treated cells, PMNP-SAB@RBCM-treated cells or PMNP-SAB@RTM-treated cells was significantly lower (Fig. 2C and D). This result further confirms the ability of RBCM or hybrid membrane-encapsulated nanoparticles to evade phagocytosis by macrophages. In addition, to verify the homologous targeting ability of the synthesized PMNP-SAB@RTM, DiL-labeled PMNP-SAB@RTM was incubated with different cells (4T1, TAFs, and

NIH3T3 cells) for 3 h. Laser confocal microscopy revealed that DiL-labeled PMNP-SAB@RTM (red) aggregated in TAFs (blue), indicating that PMNP-SAB@RTM was more readily taken up by TAFs because of the homologous targeting ability of TAFM (Fig. 2E). In contrast, PMNP-SAB@RTM was almost absent in NIH3T3 and 4T1 cells. We also measured the uptake of PMNP-SAB@RTM by various cells via flow cytometry. The results revealed that the average fluorescence intensity in TAFs treated with PMNP-SAB@RTM was significantly greater than that in NIH3T3 and 4T1 cells, further confirming the homologous targeting ability of PMNP-SAB@RTM (Fig. 2F and G). Next, we used western blotting to determine the expression of α-SMA in TAFs after treatment with different preparations (Fig. 2H and I). TGF-β1 can successfully activate NIH3T3 cells into TAFs. Both SAB and PMNP-SAB@RTM downregulated α-SMA expression, indicating that they inhibited the activation of TAFs ($p = 0.0230$, $p < 0.0001$).

3.3. Anticancer effect in vitro

CCK-8 was used to evaluate the cytotoxicity of nanoparticles towards TAFs. As shown in Fig. 3A, PMNPs did not exhibit significant cytotoxicity in the range of 0–200 μM, indicating excellent biocompatibility of PMNPs. The viability of TAFs treated with SAB, PMNP-SAB, and PMNP-SAB@RTM remained above 90 % within the range of 0–100 μM. It is worth noting that the cell viability of SAB, PMNP-SAB, and PMNP-SAB@RTM significantly decreased at a concentration of 200 μM, indicating that SAB has certain cytotoxicity when the concentration exceeds 100 μM. Therefore, a SAB concentration of 100 μM was selected for subsequent *in vitro* cell experiments. To investigate the therapeutic effects of different formulations, apoptosis of cancer cells was detected by flow cytometry after AV/PI staining. Compared with the control group, there was no significant change in cell apoptosis in the PMNPs group, further demonstrating the good biocompatibility of PMNPs (Fig. 3B). As expected, the apoptosis of SAB, PMNP-SAB, PMNP-SAB@RTM, BMS-1, and BMS-1+PMNP-SAB@RTM groups was significantly higher than that of the control group. The apoptosis of 4T1 cells in the PMNP-SAB group was significantly higher than that in the SAB group, indicating that nanotechnology can enhance the anticancer effect of SAB. Compared with the PMNP-SAB group, the apoptosis of cells in the PMNP-SAB@RTM group was significantly increased, indicating that the mixed membrane modification enhanced the anti-tumor effect of the nanoparticles. In addition, the apoptosis rate of 4T1 cells treated with the combination of BMS-1 and PMNP-SAB@RTM was higher than that treated with BMS-1 or PMNP-SAB@RTM alone. These results highlighted the synergistic effect of combination therapy.

3.4. Pharmacokinetics and biological distribution in vivo

Before exploring the therapeutic effect of PMNP-SAB@RTM on TNBC, we first evaluated its pharmacokinetics in tumor-bearing mice (Fig. 4A). The fluorescent dye DIR was loaded into the magnetic nanoparticles instead of SAB to enable direct observation of the *in vivo* behavior of the nanoparticles. DIR was monitored in the plasma of model mice at various time points following a single tail vein injection (Fig. 4B and C). No red fluorescence of DIR was observed after 10 h. Compared with the free DIR, the half-life of PMNP-DIR@RTM and PMNP-DIR@RTM + MF significantly increased, while the half-life of PMNP-DIR did not change significantly (Fig. 4D). The significant increase in the half-life of PMNP-DIR@RTM and PMNP-DIR@RTM + MF
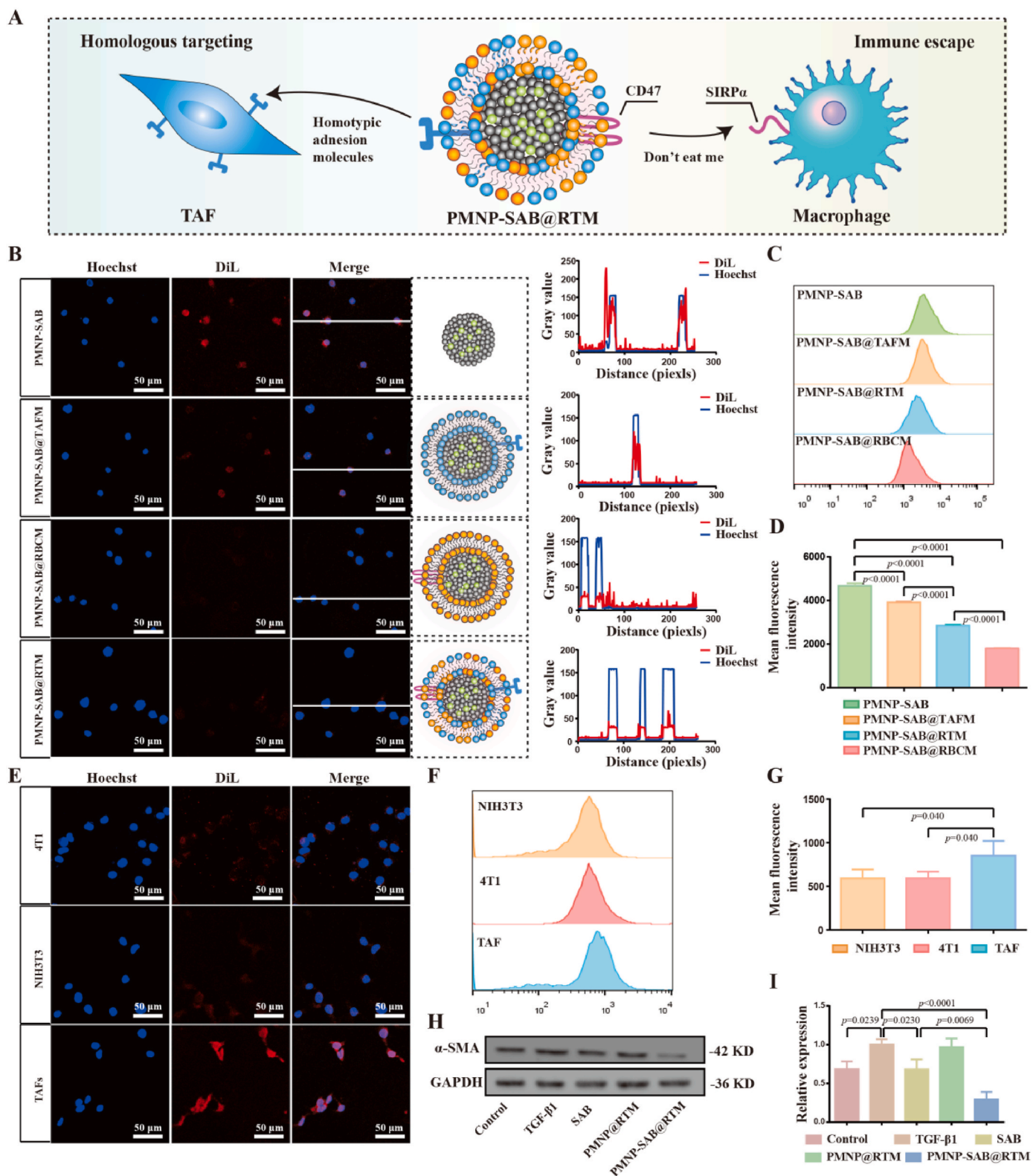
Fig. 2. *In vitro* cellular uptake and targeting ability of different formulations. (A) Schematic illustration of the immune escape and homologous targeting of PMNP-SAB@RTM. (B) Laser confocal microscopy images and fluorescence overlap curves of DiL-labeled nanoparticles after 1 h of coincubation with RAW264.7 cells. Scale bar = 100 μm. (C and D) Flow cytometric analysis of different formulations and RAW264.7 cells coincubated for 1 h (n = 3). (E) Laser confocal microscopy images and fluorescence overlap curves of DiL-labeled PMNP-SAB@RTM after 3 h of coincubation with different cells (4T1, TAF, and NIH3T3 cells). Scale bar = 50 μm. (F and G) Flow cytometric analysis of PMNP-SAB@RTM and different cells (4T1, TAF, and NIH3T3 cells) coincubated for 3 h (n = 3). (H) Western blot analysis of α-SMA expression after treatment of TAFs with different treatments. (I) Western blot quantification of α-SMA expression in TAFs after treatment with different formulations (n = 3).
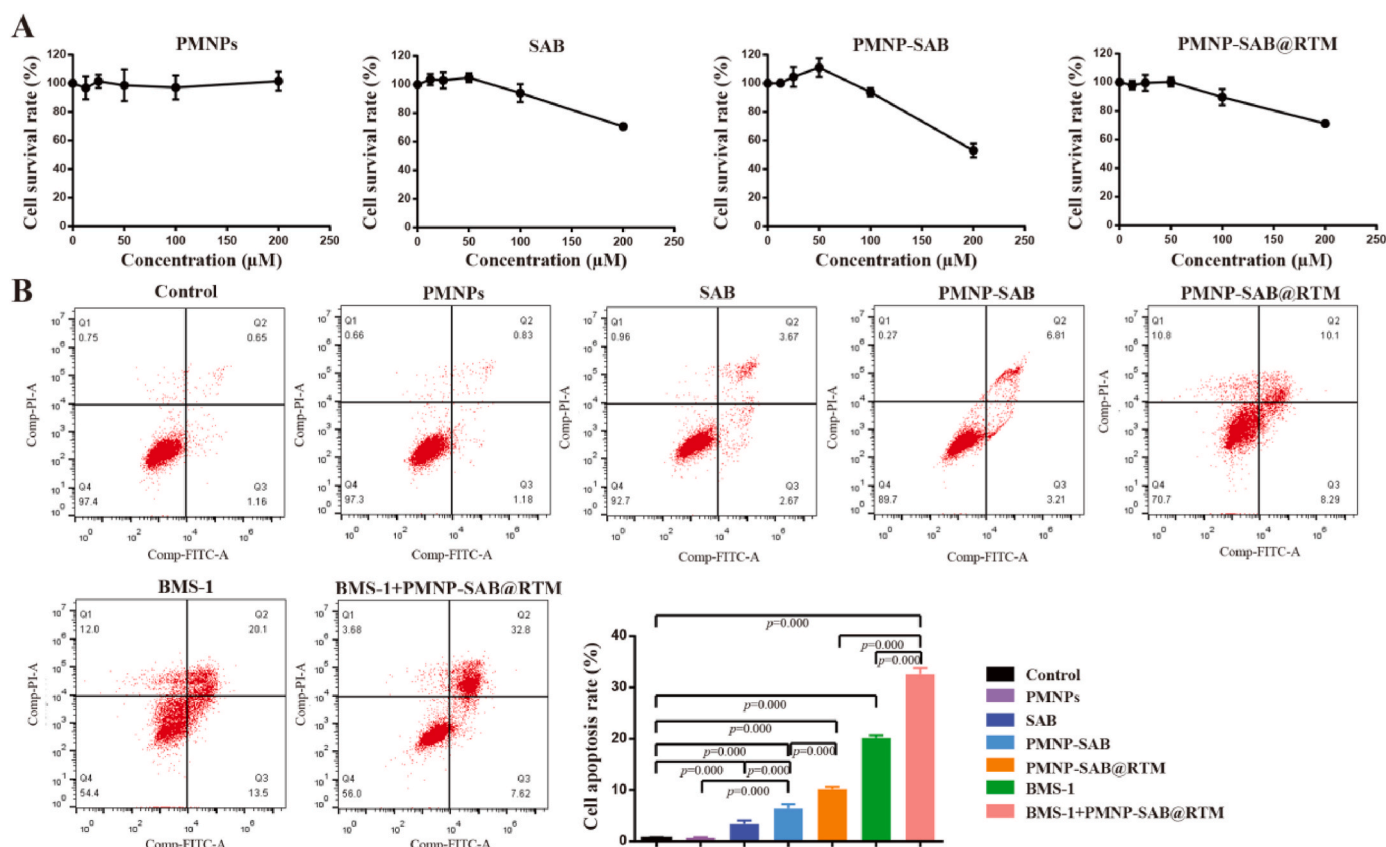
Fig. 3. *In vitro* anti-tumor efficacy of different formulations. (A) TAFs viability of incubation with different treatments for 24 h (n = 6). (B) Cell apoptosis of 4T1 cells treated with different groups (n = 3).

suggests that RBCM camouflage contributes to nanoparticle evasion of immune recognition and subsequent clearance in the bloodstream. To confirm whether TAFM artifacts promoted the accumulation of PMNP-DIR@RTM in tumors, the distribution of DIR fluorescence *in vivo* in tumor model mice was monitored in real time. As shown in Fig. 4E, PMNP-DIR@RTM was able to detect a strong fluorescent signal in the tumor 12 h after administration. Notably, the PMNP-DIR@RTM group exhibited increased aggregation of fluorescent signals within the tumor when exposed to an applied MF. The major organs of the mice were isolated for fluorescence imaging 24 h after injection. The results revealed that the fluorescence of free DIR and PMNP-DIR was detectable in the liver and spleen, while the fluorescent signal in the tumors was weaker than in other groups (Fig. 4F and G). These findings suggest that the liver and spleen are the main organs involved in free DIR and PMNP-DIR accumulation, which is consistent with the findings of other studies [52]. Stronger fluorescence remained in the tumors of the PMNP-DIR@RTM group and the PMNP-DIR@RTM + MF group at 24 h postinjection (*p* = 0.0142, *p*=0.0002). Among them, the strongest fluorescence was observed in the tumors of the PMNP-DIR@RTM + MF group (*p* = 0.013). In addition, the concentrations of SAB and PMNP-SAB@RTM were measured *in vivo* at different times. As expected, nanoparticles increased the blood concentration and circulation time of SAB *in vivo* (Fig. 4H). These results indicate that PMNP-DIR@RTM is characterized by a long blood retention time, homologous targeting ability, and magnetic targeting ability, demonstrating multifunctional hybridization.

3.5. Combined antitumor effects of PMNP-SAB@RTM and BMS-1 in vivo

To further evaluate the synergistic antitumor effect of PMNP-SAB@RTM and BMS-1 (PD-1/PD-L1 inhibitor), we established "cold"

tumor models using 4T1 cells (Fig. 5A). Tumor-bearing mice were subjected to different treatments: saline, BMS-1, PMNP-SAB@RTM, PMNP-SAB@RTM and BMS-1 in combination, and PMNP-SAB@RTM and BMS-1 in combination with MF. Tumor growth and mouse body weight trends were monitored throughout the course of drug administration. Treatment with BMS-1, PMNP-SAB@RTM alone, or the combination of BMS-1 and PMNP-SAB@RTM significantly inhibited tumor growth (Fig. 5B and C). Compared with treatment with BMS-1 or PMNP-SAB@RTM alone, the combination of BMS-1 and PMNP-SAB@RTM significantly inhibited tumor growth and reduced tumor weight. Notably, the combined antitumor effect of BMS-1 and PMNP-SAB@RTM was optimal in the presence of an applied MF. These results suggest that the magnetic targeting ability of PMNP-SAB@RTM enables greater drug accumulation in the tumor, leading to an antitumor response. Similarly, the tumor suppression rates were approximately 33.84 %, 33.08 %, 63.15 %, 28 %, and 91.27 % in the BMS-1, PMNP-SAB@RTM, BMS-1+PMNP-SAB@RTM, and BMS-1+PMNP-SAB@RTM + MF groups, respectively (Fig. 5D). The tumor growth curves revealed the fastest tumor growth in the model group (Fig. 5E). Slight slowing of tumor growth was observed after single BMS-1 or PMNP-SAB@RTM treatment. The tumor growth rate was significantly reduced by the combination of PMNP-SAB@RTM and BMS-1 (*p* = 0.006), and the inhibition of the tumor growth rate was most pronounced with the combination treatment in the presence of an applied MF (*p* = 0.002). Notably, the inhibition of tumor growth after combination therapy was significantly greater than that after single BMS-1 or PMNP-SAB@RTM treatment (*p* = 0.033, *p* = 0.008). These results suggest that the combination of PMNP-SAB@RTM and BMS-1 can significantly enhance efficacy. In addition, there was no significant difference in the body weights of the mice in each group during the treatment period (Fig. 5F). The survival rate of tumor-bearing mice in the BMS-1+PMNP-SAB@RTM + MF group was
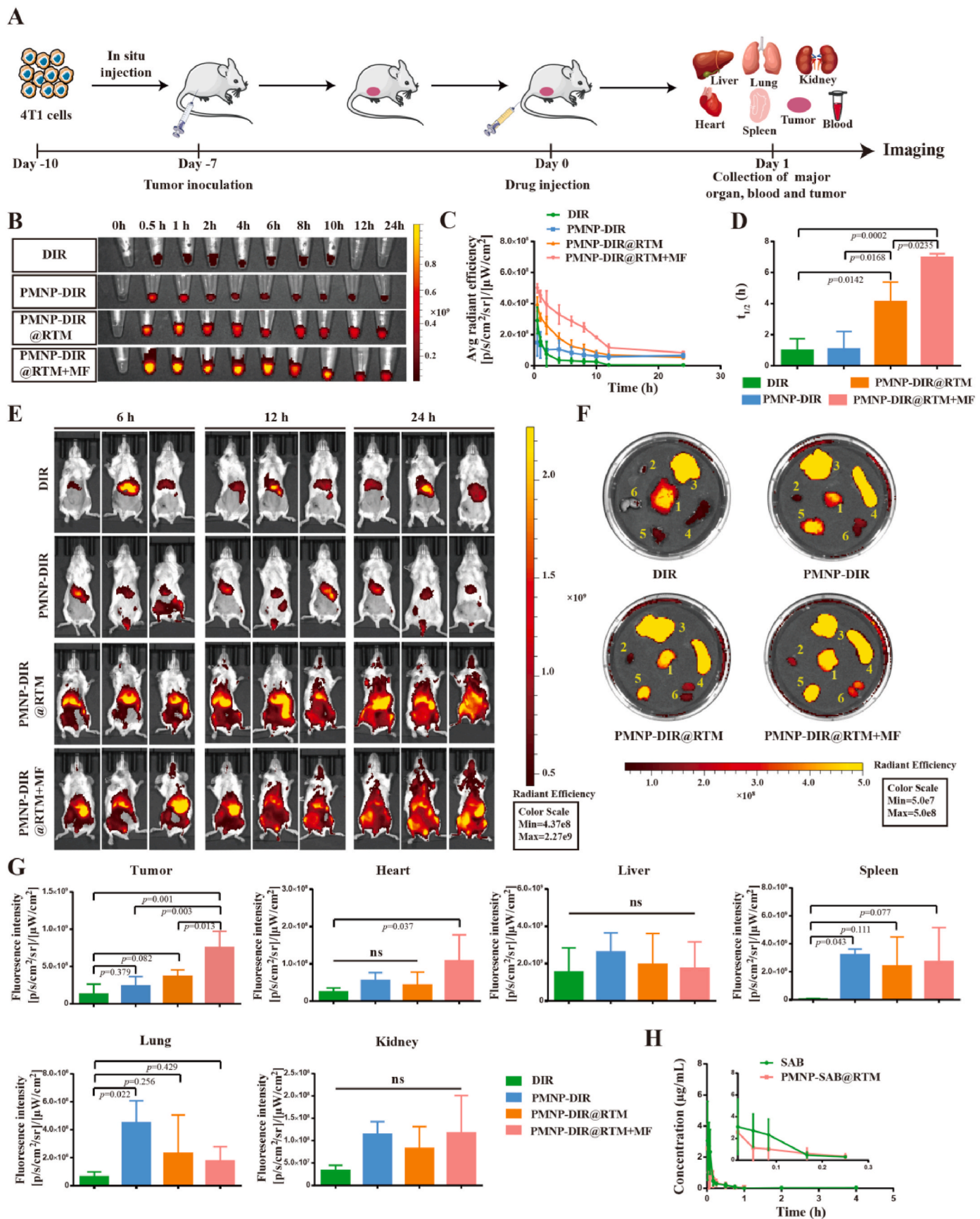
(caption on next page)

Fig. 4. Pharmacokinetics and biological distribution of PMNP-SAB@RTM. (A) Schematic diagram of the administration of different formulations. (B) Fluorescence images of DIR in plasma at different time points after administration. (C) Pharmacokinetic profiles of DIR, PMNP-DIR@RTM, and PMNP-DIR@RTM + MF in tumor-bearing mice (n = 3). (D) The half-lives of DIR, PMNP-DIR@RTM, and PMNP-DIR@RTM + MF *in vivo*. (E) *In vivo* fluorescence images of tumor-bearing mice at 2, 6, and 12 h after a single tail vein injection of free DIR, PMNP-DIR@RTM or PMNP-DIR@RTM + MF. (F) Fluorescence images of tumors and major organs 24 h after a single tail vein injection of free DIR, PMNP-DIR@RTM or PMNP-DIR@RTM + MF (1: tumor, 2: heart, 3: liver, 4: spleen, 5: lung, 6: kidney). (G) Quantification of DIR accumulation in tumors and major organs 24 h after a single tail vein injection of free DIR, PMNP-DIR@RTM or PMNP-DIR@RTM + MF (n = 3). (H) Pharmacokinetic profiles of SAB and PMNP-DIR@RTM (n = 5).

much higher than that in the model, BMS-1, PMNP-SAB@RTM, and BMS-1+PMNP-SAB@RTM groups (Fig. 5G). This result indicated that BMS-1+PMNP-SAB@RTM + MF significantly prolonged the survival time of tumor-bearing mice. After confirming that PMNP-SAB@RTM enhanced the antitumor effect of BMS-1, its impact on α-SMA expression was further explored. As shown in Fig. 5H and I, the expression of α-SMA was significantly inhibited in all the treatment groups, indicating that TAF activation was inhibited across all the treatment groups (*p* < 0.0001). Compared with treatment with BMS-1 or PMNP-SAB@RTM alone, the combination of BMS-1 and PMNP-SAB@RTM significantly inhibited α-SMA expression (*p* = 0.0035, *p* = 0.0435). The applied MF enhanced the inhibition of α-SMA expression by increasing the accumulation of SAB in the tumor.

3.6. Increased ECM deposition and cell apoptosis in vivo

TAFs are important players in the failure of tumor immunotherapy. Collagen produced by TAFs forms a physical barrier that hinders T-cell infiltration and inhibits the penetration of antitumor drugs and nanoparticles in tumors. Therefore, we first investigated whether PMNP-SAB@RTM could reduce collagen deposition after TAFs were inhibited. Masson's trichrome staining revealed severe ECM deposition in the model group (Fig. 6A). Compared with the model group, the BMS-1, PMNP-SAB@RTM, BMS-1+PMNP-SAB@RTM, and BMS-1+PMNP-SAB@RTM + MF groups presented reductions of 25 %, 37 %, 60 % and 80 %, respectively (Fig. 6B). Under the effect of the applied MF, the combination of PMNP-SAB@RTM and BMS-1 could minimize ECM deposition, suggesting that the magnetic targeting ability of PMNP-SAB@RTM could enable more drug accumulation at the tumor site. TUNEL staining was used to observe tumor cell apoptosis. As shown in Fig. 6C, tumor cell apoptosis was lower in the model group than in the BMS-1 and PMNP-SAB@RTM groups, but apoptosis occurred at the tumor edge (*p* < 0.001, *p* = 0.006). The reason for this may be that the physical barrier created by TAFs prevents antitumor drugs and nanoparticles from entering the tumor interior to kill tumor cells. The combination of PMNP-SAB@RTM and BMS-1 significantly increased tumor cell apoptosis, and apoptosis mostly occurred within the tumor (Fig. 6C and D). These results suggest that PMNP-SAB@RTM reduces ECM deposition by inhibiting TAF activation, which breaks down the physical barrier in the tumor to promote BMS-1 penetration and ultimately kills cells inside the tumor. In addition, the combined induction of apoptosis in tumor cells by PMNP-SAB@RTM and BMS-1 was optimal in the presence of an applied MF (*p* < 0.0001), indicating that the applied MF allowed more PMNP-SAB@RTM to accumulate at the tumor site to play a role. H&E staining was used to explore the antitumor mechanisms of PMNP-SAB@RTM and BMS-1. The results revealed that the tumor tissue in the model group was tightly structured, indicating that little cell necrosis occurred (Fig. 6E). After treatment with PMNP-SAB@RTM or BMS-1 alone, the tumor tissue showed slight structural sparing, indicating necrosis of some cells in the tumor. In contrast, the tumor tissue in the BMS-1+PMNP-SAB@RTM group and the BMS-1+PMNP-SAB@RTM + MF group was sparsely structured and contained many vacuolated necrotic cells. Among them, tumor cell necrosis was more severe in the BMS-1+PMNP-SAB@RTM + MF group. In addition, Ki67 staining of tumors in the BMS-1+PMNP-SAB@RTM + MF group showed the least cell proliferation. These results suggest that PMNP-SAB@RTM and BMS-1 can be more effectively targeted to penetrate tumors to kill tumor cells and exert synergistic antitumor effects with the assistance of an applied MF.

### 3.7. "Cold" tumor immunosuppressive microenvironment remodeling

TAFs can not only build physical barriers to hinder T-cell infiltration but also promote immune escape by recruiting immunosuppressive cells. Therefore, we further analyzed the changes in the immune cell population via flow cytometry. Tregs lead to immune suppression by inhibiting the maturation of DCs and reducing the activity of effector T cells. M2 macrophages interfere with antitumor immune activation by recruiting Tregs. In contrast, M1 macrophages can initiate antitumor responses by releasing proinflammatory factors. Mature T cells are composed of CD4 (+) and CD8 (+) cells, which can kill cancer cells after specific recognition and binding. Therefore, we analyzed the effects of the combination of PMNP-SAB@RTM and BMS-1 on CD4$^+$ and CD8$^+$ T cells, M1 macrophages, M2 macrophages, and Tregs. As shown in Fig. 7A and B, BMS-1 promoted the upregulation of CD8$^+$ T cells but had no significant effect on CD4$^+$ T cells. In contrast, PMNP-SAB@RTM promoted the upregulation of CD4$^+$ T cells but had no effect on CD8$^+$ T cells. Both BMS-1 and PMNP-SAB@RTM combination therapy significantly increased CD4$^+$ T and CD8$^+$ T levels (*p* = 0.0204, *p* = 0.0004). In addition, the level of CD4$^+$ T cells was greater in the combined treatment group than in the control group under the effect of an applied MF, suggesting that this treatment effectively promoted the infiltration of immune cells (*p* < 0.0001). Compared with those in the single BMS-1 or PMNP-SAB@RTM treatment groups, the proportion of M1/M2 macrophages was significantly greater and the proportion of Treg cells was lower after combination treatment under an applied MF. These results suggest that combination therapy inhibited the infiltration of antitumor immunosuppressive cells. To further investigate the mechanism by which PMNP-SAB@RTM promote immune cell anti-tumor responses, the expression of cytokines was measured. The CXCL9, CXCL10, and CXCL12 secreted by TAFs can block T cell infiltration [53,54]. Compared with the model group, PMNP-SAB@RTM significantly reduced the levels of CXCL9 and CXCL12 (Fig. 7C). However, both PMNP-SAB@RTM and BMS-1 had no effect on the level of CXCL10. These results suggestd that PMNP-SAB@RTM may promote T cell infiltration by inhibiting the secretion of CXCL9, and CXCL12 by TAFs. Interleukin-6 (IL-6) plays an important role in promoting tumor cell proliferation and metastasis. Compared with the model group, all treatment groups downregulated the expression of IL-6. Tumor necrosis factor-α (TNF-α) and interferon-γ (IFN-γ) are common pro-inflammatory factors in the tumor microenvironment. The secretion level of TNF-α was highest in the BMS-1+PMNP-SAB@RTM + MF group, indicating that the immune response was activated. Although PMNP-SAB@RTM promoted the secretion of IFN-γ, BMS-1 significantly inhibited the level of IFN-γ. Therefore, the secretion of IFN-γ decreased after combination therapy, but showed an upward trend compared to the BMS-1 group. Overall, PMNP-SAB@RTM can provide a beneficial immune microenvironment for BMS-1.

3.8. Biosafety evaluation

To assess the biosafety of the nanoparticles, hemolytic assays and blood biochemical tests were performed. As shown in Fig. 8A and B, there were slight hemolysis observed in both low and high concentrations of SAB. As expected, the hemolysis rates of PMNPs, PMNP-SAB, and PMNP-SAB@RTM were less than 5 % at concentrations up to 50
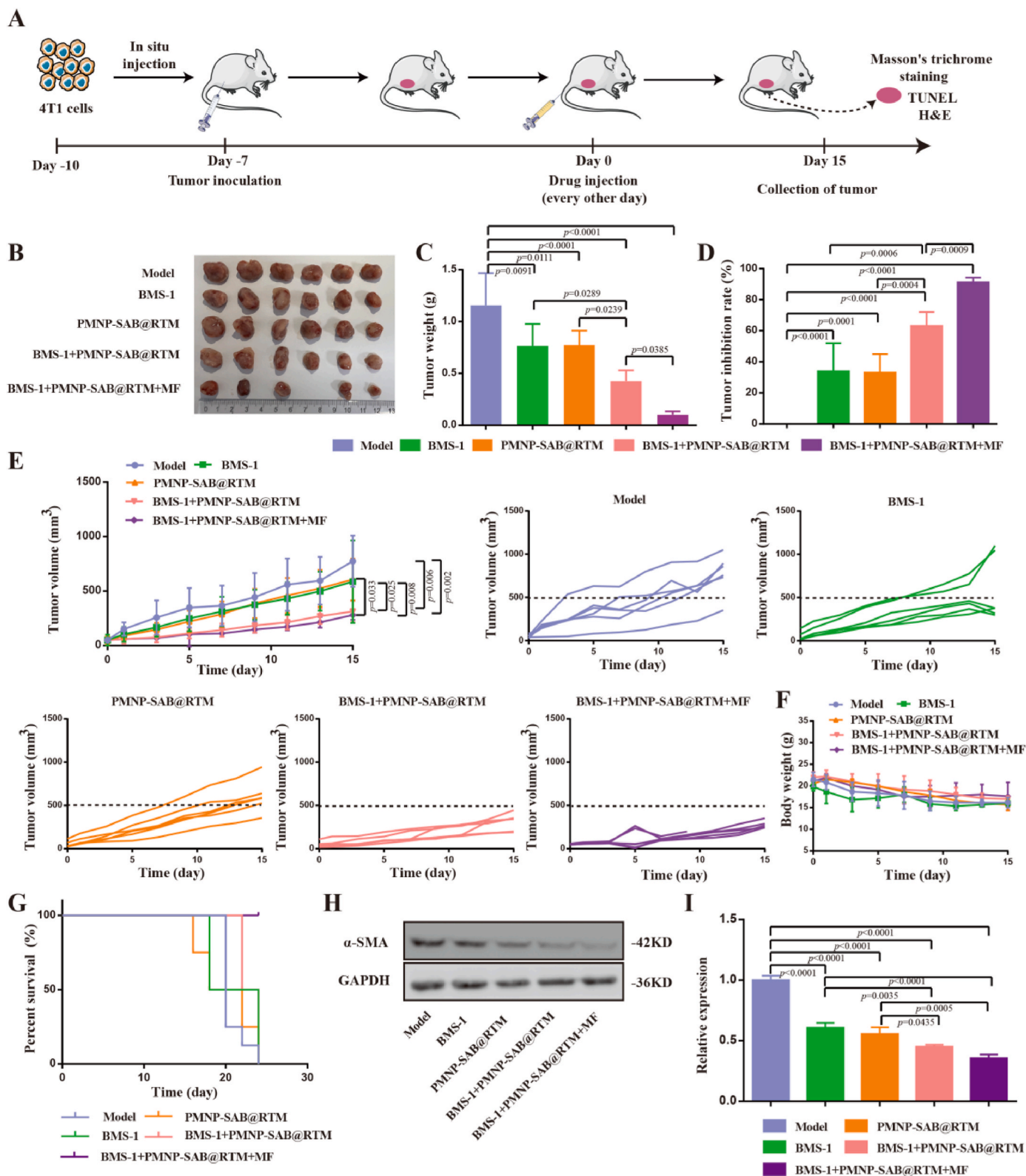
Fig. 5. PMNP-SAB@RTM and BMS-1 synergistically inhibited tumor growth. (A) Schematic diagram of the administration of different formulations. (B) Images of tumors from different treatment groups. (C) Tumor weight after treatment in each group (n = 6). (D) Tumor inhibition rate (n = 6). (E) Curves of tumor growth for each group (n = 6). (F) Curves of body weight changes in the mice (n = 6). (G) Survival percentage curves of tumor-bearing mice after treatment in each group (n = 8). (H) α-SMA expression was determined by western blotting. (I) Quantitative analysis of α-SMA expression (n = 3).
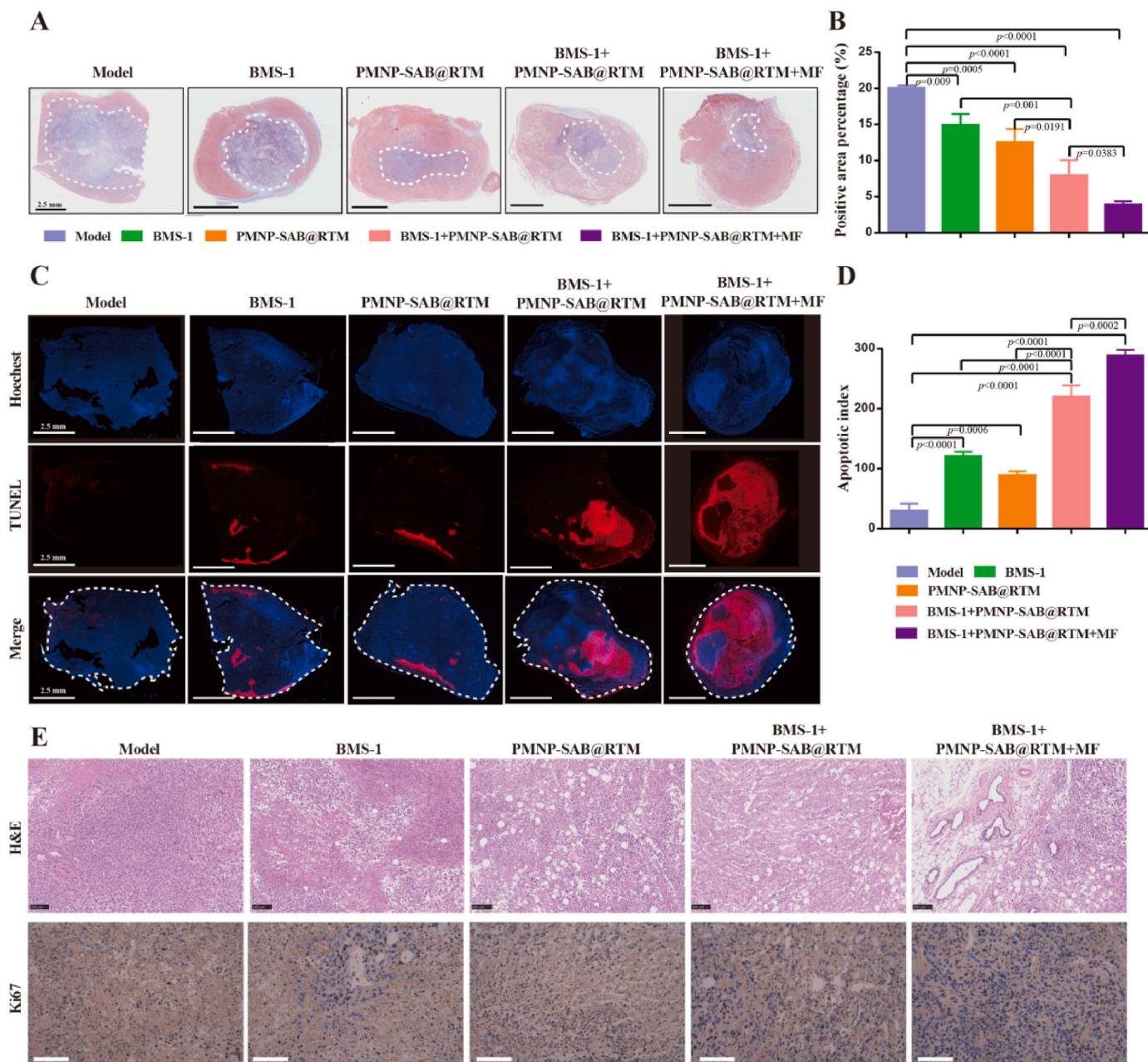
Fig. 6. BMS-1 and PMNP-SAB@RTM synergistically reduced the ECM and promoted the apoptosis of tumor cells. (A) Masson's trichrome staining was used to observe collagen deposition in each group after treatment. (B) Quantitative analysis of collagen deposition (n = 3). (C) TUNEL staining of tumors from each group after treatment. (D) Quantitative analysis of apoptosis (n = 3). (E) H&E and Ki67 staining of the different treatment groups. Scale bar = 100 μm.

μg/mL (Fig. 8A and B). These results indicated that loading SAB into multifunctional nanoparticles can reduce the hemolysis rate of SAB, suggesting that multifunctional nanoparticles are a promising nanoplatform. Major organs and serum were collected from tumor-bearing mice after they received multiple injections of various formulations. H&E staining of major organs revealed a normal tissue structure after treatment with different preparations, suggesting that the designed PMNP-SAB@RTM was not significantly toxic (Fig. 8C). In addition, the collected serum was used to test indicators of liver and kidney function, as well as cardiac function. As shown in Fig. 8D, alanine aminotransferase (ALT), aspartate aminotransferase (AST), creatinine (CRE), blood urea nitrogen (BUN), and creatine kinase (CK) levels were not significantly different between the groups and were all within the normal range. These results indicated that the prepared PMNP-SAB@RTM exhibited good biosafety *in vivo*.

4. Conclusion

In this study, a hybrid membrane nanodelivery system with dual functions of immune escape and homologous targeting was developed, which delivers SAB to TAFs to drive the transformation of "cold" tumors into "hot" tumors, enhancing the therapeutic ability of BMS-1. The fusion of RBCM and TAFM on the surface of nanoparticles enhances the circulation time of SABs *in vivo*, allowing them to accumulate more in TAFs and altering the immune "cold" microenvironment, which cannot be achieved by free SAB. In addition, the use of porous magnetic nanoparticles as the core of the delivery system can target the TME under the action of an external MF, further improving the aggregation of SABs in the TME. The combination of PMNP-SAB@RTM and BMS-1 increased antitumor efficiency and increased T-cell infiltration in the TME, reducing the recruitment of immunosuppressive cells. These findings
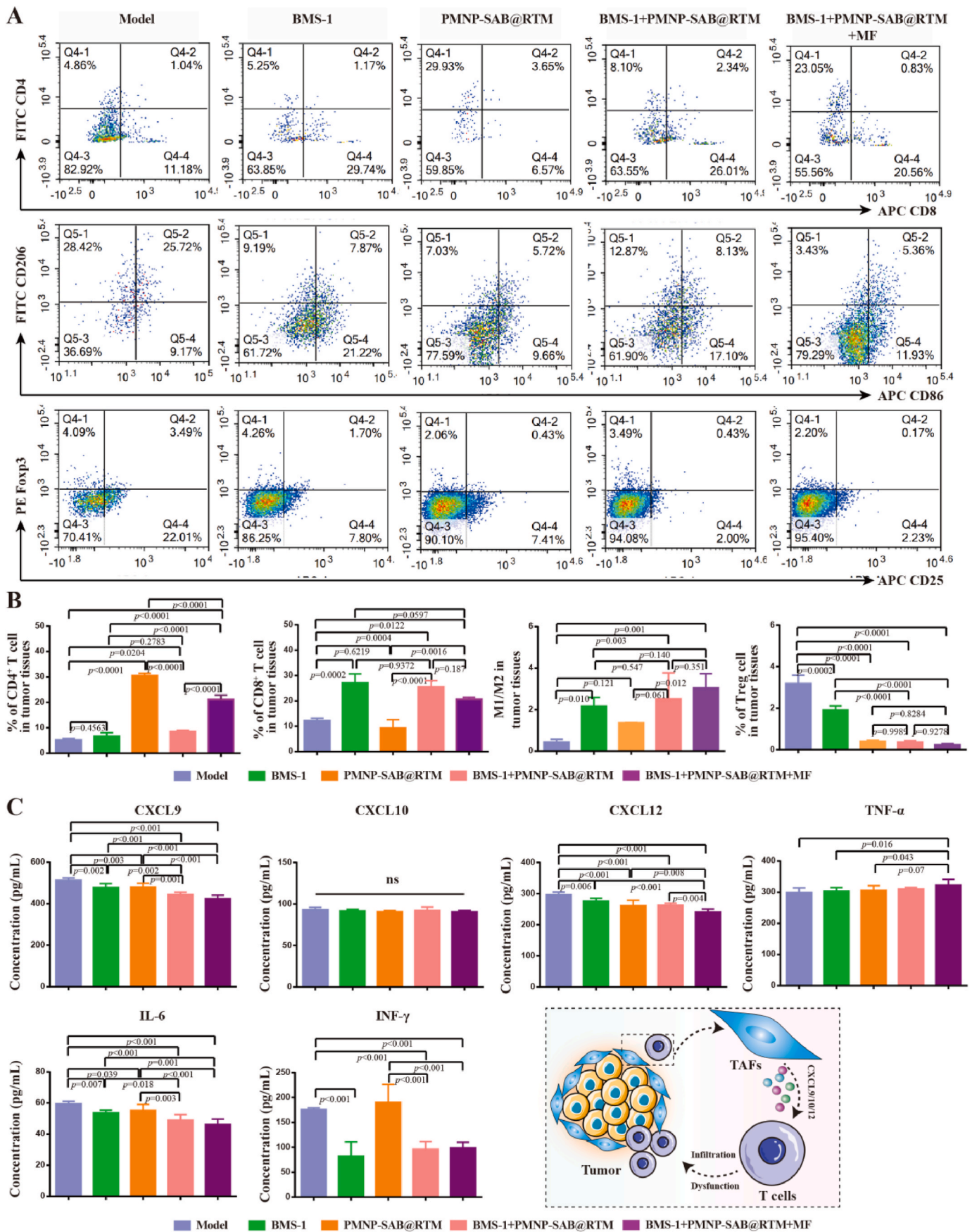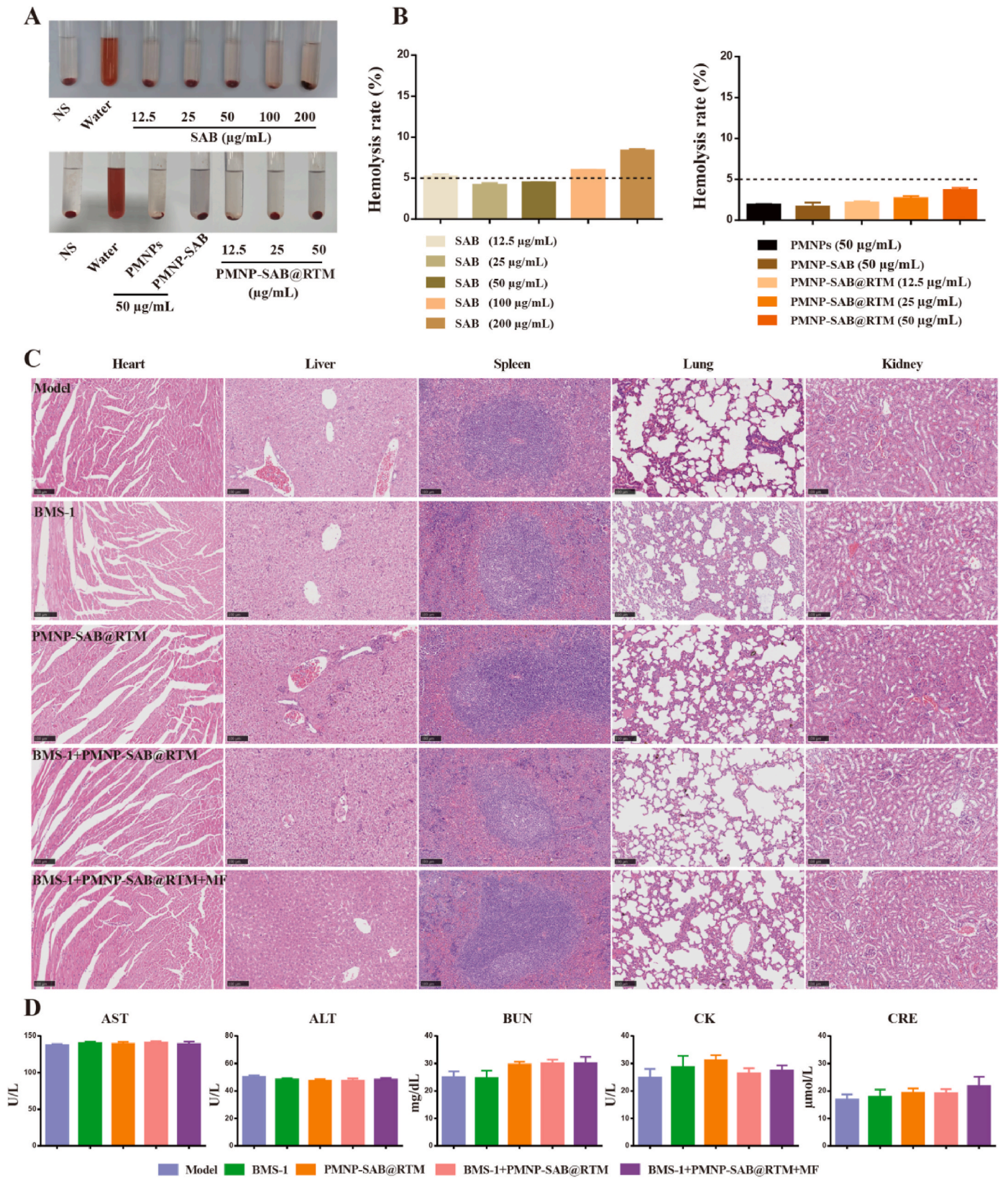
Fig. 7. Flow cytometry evaluation of the tumor immune microenvironment. (A) Flow cytometry analysis of the proportions of immune cells in tumors. (B) Quantification of immune cell infiltration (n = 3). (C) Cytokine levels in tumors (n = 5).

Fig. 8. *In vivo* biosafety evaluation. (A) Images of hemolysis after incubation with different formulations. (B) Hemolysis rate after incubation with different formulations (n = 5). (C) H&E-stained images of major organs. Scale bar = 100 μm. (D) Biochemical indices of hepatic (ALT, AST), renal (BUN, CRE) and cardiac (CK) function (n = 3).

indicate that PMNP-SAB@RTM can enhance the immunotherapy effect of BMS-1 by inhibiting TAFs to drive the transformation of "cold" tumors into "hot" tumors. In summary, this collaborative therapeutic approach provides new ideas for the treatment of immune "cold" tumors.

CRediT authorship contribution statement

Nuo Cheng: Writing – original draft, Visualization, Methodology, Data curation. **Qianqian Zhou:** Writing – original draft, Visualization, Methodology. **Zongfang Jia:** Visualization, Methodology. **Yang Mu:** Methodology. **Sheng Zhang:** Validation, Data curation, Conceptualization. **Lei Wang:** Writing – review & editing, Validation. **Yunna Chen:** Writing – review & editing, Visualization, Funding acquisition.

Declaration of competing interest

We declare that we have no financial and personal relationships with other people or organizations that can inappropriately influence our work, there is no professional or other personal interest of any nature or kind in any product, service and/or company that could be construed as influencing the position presented in, or the review of, the manuscript entitled.

Acknowledgments

Data availability

Data will be made available on request.

References

[1] L. Yin, J.J. Duan, X.W. Bian, S.C. Yu, Triple-negative breast cancer molecular subtyping and treatment progress, Breast Cancer Res. 22 (1) (2020).

[2] F. Derakhshan, J.S. Reis, Pathogenesis of triple-negative breast cancer, Annu Rev Pathol-Mech 17 (2022) 181–204.

[3] Y. Li, H.J. Zhang, Y. Merkher, L. Chen, N. Liu, S. Leonov, Y.H. Chen, Recent advances in therapeutic strategies for triple-negative breast cancer, J. Hematol. Oncol. 15 (1) (2022).

[4] A.M. Karim, J.E. Kwon, T. Ali, J. Jang, I. Ullah, Y.G. Lee, D.W. Park, J. Park, J. W. Jeang, S.C. Kang, Triple-negative breast cancer: epidemiology, molecular mechanisms, and modern vaccine-based treatment strategies, Biochem. Pharmacol. 212 (2023).

[5] H. O'Rourke, C. Hart, R.H. De Boer, Current usage of pembrolizumab in triple negative breast cancer (TNBC), Expert Rev Anticanc 24 (5) (2024) 253–261.

[6] E. Agostinetto, A. Losurdo, G. Nader-Marta, A. Santoro, K. Punie, R. Barroso, L. Popovic, C. Solinas, M. Kok, E. de Azambuja, M. Lambertini, Progress and pitfalls in the use of immunotherapy for patients with triple negative breast cancer, Expet Opin. Invest. Drugs 31 (6) (2022) 567–591.

[7] J.Y. Wu, W. Wang, L. Gao, X.Y. Shao, X.J. Wang, Cyclin-dependent kinase inhibitors enhance programmed cell death protein 1 immune checkpoint blockade efficacy in triple-negative breast cancer by affecting the immune microenvironment, Cancer-Am Cancer Soc 130 (2024) 1449–1463.

[8] S.S. Said, W.N. Ibrahim, Breaking barriers: the promise and challenges of immune checkpoint inhibitors in triple-negative breast cancer, Biomedicines 12 (2) (2024).

[9] T. Ugai, Q. Yao, S. Ugai, S.J. Ogino, Advancing precision oncology: insights into the tumor microenvironment and immunotherapy outcomes, Innovation 5 (4) (2024).

[10] Z.C. Xiao, Z.W. Su, S.S. Han, J.S. Huang, L.T. Lin, X.T. Shuai, Dual pH-sensitive nanodrug blocks PD-1 immune checkpoint and uses T cells to deliver NF-κB inhibitor for antitumor immunotherapy, Sci. Adv. 6 (6) (2020).

[11] Z.C. Xiao, T. Li, X.Y. Zheng, L.T. Lin, X.B. Wang, B. Li, J.J. Huang, Y. Wang, X. T. Shuai, K.S. Zhu, Nanodrug enhances post-ablation immunotherapy of hepatocellular carcinoma via promoting dendritic cell maturation and antigen presentation, Bioact. Mater. 21 (2022) 57–68.

[12] Z.C. Xiao, Y.J. Cai, X.B. Wang, L.J. Hu, M.Z. Lin, K.S. Zhu, Y. Wang, X.T. Shuai, Nanodrug Simultaneously Regulates Stromal Extracellular Matrix and Glucose Metabolism for Effective Immunotherapy against Orthotopic Pancreatic Cancer, Nano Today, vol. 44, 2022.

[13] Y. Xiao, D. Ma, S. Zhao, C. Suo, J.X. Shi, M.Z. Xue, M. Ruan, H. Wang, J.J. Zhao, Q. Li, P. Wang, L.M. Shi, W.T. Yang, W. Huang, X. Hu, K.D. Yu, S.L. Huang, F. Bertucci, Y.Z. Jiang, Z.M. Shao, A.B.C.C. Grp, Multi-omics profiling reveals distinct microenvironment characterization and suggests immune escape mechanisms of triple-negative breast cancer, Clin. Cancer Res. 25 (16) (2019) 5002–5014.

[14] Y.J. Tang, G.Z. Cui, H.C. Liu, Y. Han, C.J. Cai, Z.Y. Feng, H. Shen, S. Zeng, Converting "cold" to "hot": epigenetics strategies to improve immune therapy effect by regulating tumor-associated immune suppressive cells, Cancer Commun. 44 (6) (2024) 601–636.

[15] G.R. Khosravi, S. Mostafavi, S. Bastan, N. Ebrahimi, R.S. Gharibvand, N. Eskandari, Immunologic tumor microenvironment modulators for turning cold tumors hot, Cancer Commun. 44 (5) (2024) 521–553.

[16] T.C. Guo, J.F. Xu, Cancer-associated fibroblasts: a versatile mediator in tumor progression, metastasis, and targeted therapy, Cancer Metastasis Rev. 43 (3) (2024) 1095–1116.

[17] S. Singh, A.P. Singh, R. Mitra, Cancer-associated fibroblasts: major co-conspirators in tumor development, Cancers 16 (1) (2024).

[18] X.Y. Meng, Z.L. Liu, L. Deng, Y.Z. Yang, Y.C. Zhu, X.Y. Sun, Y.Q. Hao, Y. He, J. K. Fu, Hydrogen therapy reverses cancer-associated fibroblasts phenotypes and remodels stromal microenvironment to stimulate systematic anti-tumor immunity, Adv. Sci. 11 (28) (2024).

[19] Y.S. Wu, Z.Y. Yi, J. Li, Y.X. Wei, R. Feng, J.Z. Liu, J.F. Huang, Y.R. Chen, X. Y. Wang, J.Z. Sun, X.D. Yin, Y.H. Li, J.Y. Wan, L. Zhang, J. Huang, H.M. Du, X. Y. Wang, Q. Li, G.S. Ren, H.Z. Li, FGFR blockade boosts T cell infiltration into triple-negative breast cancer by regulating cancer-associated fibroblasts, Theranostics 12 (10) (2022) 4564–4580.

[20] Y. Liu, Z.Z. Xun, K. Ma, S.H. Liang, X.Y. Li, S. Zhou, L.M. Sun, Y.F. Liu, Y.H. Du, X. Y. Guo, T.M. Cui, H.R. Zhou, J.Z. Wang, D.L. Yin, R.P. Song, S.G. Zhang, W. Cai, F. Z. Meng, H.R. Guo, B. Zhang, D. Yang, R.J. Bao, Q.S. Hu, J.B. Wang, Y.Q. Ye, L. X. Liu, Identification of a tumour immune barrier in the HCC microenvironment that determines the efficacy of immunotherapy, J. Hepatol. 78 (4) (2023) 770–782.

[21] R. Yan, P. Moresco, B. Gegenhuber, D.T. Fearon, T cell-mediated development of stromal fibroblasts with an immune-enhancing chemokine profile, Cancer Immunol. Res. 11 (8) (2023) 1044–1054.

[22] S. Mariathasan, S.J. Turley, D. Nickles, A. Castiglioni, K. Yuen, Y.L. Wang, E. E. Kadel, H. Koeppen, J.L. Astarita, R. Cubas, S. Jhunjhunwala, R. Banchereau, Y. G. Yang, Y.H. Guan, C. Chalouni, J. Ziai, Y. Senbabaoglu, S. Santoro, D. Sheinson, J. Hung, J.M. Giltnane, A.A. Pierce, K. Mesh, S. Lianoglou, J. Riegler, R.A. D. Carano, P. Eriksson, M. Höglund, L. Somarriba, D.L. Halligan, M.S. van der Heijden, Y. Loriot, J.E. Rosenberg, L. Fong, I. Mellman, D.S. Chen, M. Green, C. Derleth, G.D. Fine, P.S. Hegde, R. Bourgon, T. Powles, TGFβ attenuates tumour response to PD-L1 blockade by contributing to exclusion of T cells, Nature 554 (7693) (2018) 544–548.

[23] Y.E. Lee, G.Y. Go, E.Y. Koh, H.N. Yoon, M. Seo, S.M. Hong, J.H. Jeong, J.C. Kim, D. Cho, T.S. Kim, S.C. Kim, E. Jun, M. Jang, Synergistic therapeutic combination with a CAF inhibitor enhances CAR-NK-mediated cytotoxicity via reduction of CAF-released IL-6, J Immunother Cancer 11 (2) (2023).

[24] A. Vienot, J.R. Pallandre, E. Renaude, J. Viot, A. Bouard, L. Spehner, M. Kroemer, S. Abdeljaoued, B. van der Woning, H. de Haard, R. Loyon, E. Hervouet, P. Peixoto, C. Borg, Chemokine switch regulated by TGF-β1 in cancer-associated fibroblast subsets determines the efficacy of chemo-immunotherapy, OncoImmunology 11 (1) (2022).

[25] M.M. Yang, C. Qin, L.L. Tao, G. Cheng, J.J. Li, F.N. Lv, N. Yang, Z.H. Xing, X. Y. Chu, X.P. Han, M.R. Huo, L.F. Yin, Synchronous targeted delivery of TGF-ß siRNA to stromal and tumor cells elicits robust antitumor immunity against triple-negative breast cancer by comprehensively remodeling the tumor microenvironment, Biomaterials 301 (2023).

[26] G. Liu, Y. Bi, L. Xue, Y. Zhang, H. Yang, X. Chen, Y. Lu, Z. Zhang, H. Liu, X. Wang, R. Wang, Y. Chu, R. Yang, Dendritic cell SIRT1-HIF1α axis programs the differentiation of CD4+ T cells through IL-12 and TGF-β1, Proc. Natl. Acad. Sci. U. S.A. 112 (9) (2015) E957–E965.

[27] X.Y. Ni, H.X. Sui, Y. Liu, S.Z. Ke, Y.N. Wang, F.G. Gao, TGF-β of lung cancer microenvironment upregulates B7H1 and GITRL expression in dendritic cells and is associated with regulatory T cell generation, Oncol. Rep. 28 (2) (2012) 615–621.

[28] Y.D. Fu, X.X. Zhou, L. Wang, W.G. Fan, S.Q. Gao, D.Y. Zhang, Z.Y. Ling, Y. G. Zhang, L.Y. Ma, F. Bai, J.M. Chen, B. Sun, P. Liu, Salvianolic acid B attenuates liver fibrosis by targeting Ecm1 and inhibiting hepatocyte ferroptosis, Redox Biol. 69 (2024).

[29] M. Meng, J.Y. Wu, Y.J. Feng, L. Lin, J. Chen, X. Pang, Y.H. Li, K. Hao, H.Y. Tian, X. S. Chen, A comprehensive strategy based on high clinical translational nanosystem for programmable immunotherapy of triple negative breast cancer, Adv Mater 36 (27) (2024).

[30] Y.N. Chen, M.R. Hu, S.W. Wang, Q. Wang, H.Y. Lu, F.L. Wang, L. Wang, D.Y. Peng, W.D. Chen, Nano-delivery of salvianolic acid B induces the quiescence of tumor-associated fibroblasts via interfering with TGF-β1/Smad signaling to facilitate chemo- and immunotherapy in desmoplastic tumor, Int. J. Pharm. (Amst.) 623 (2022).

[31] C. Qian, C.M. Yang, Y. Tang, W.W. Zheng, Y.K. Zhou, S. Zhang, M.Y. Song, P. Cheng, Z.H. Wei, C.J. Zhong, L. Wan, A.Y. Wang, Y. Zhao, Y. Lu, Pharmacological manipulation of Ezh2 with salvianolic acid B results in tumor

vascular normalization and synergizes with cisplatin and T cell-mediated immunotherapy, Pharmacol. Res. 182 (2022).

[32] M.D. Wang, P.C. Peng, Z.S. Chen, X. Deng, Nanoparticle delivery of active traditional Chinese medicine ingredients: a new strategy for the treatment of liver cancer, Curr. Pharmaceut. Biotechnol. 24 (13) (2023) 1630–1644.

[33] D.H. Wei, H. Yang, Y. Zhang, X.H. Zhang, J. Wang, X.L. Wu, J. Chang, Nano-traditional Chinese medicine: a promising strategy and its recent advances, J. Mater. Chem. B (2022).

[34] J. Wang, X. Wu, J. Chen, T. Gao, Y.M. Zhang, N. Yu, Traditional Chinese medicine polysaccharide in nano-drug delivery systems: current progress and future perspectives, Biomed. Pharmacother. 173 (2024).

[35] P.S. Zhang, J.L. Meng, Y.Y. Li, C. Yang, Y. Hou, W. Tang, McHugh, K.J.L.H. Jing, Nanotechnology-enhanced immunotherapy for metastatic cancer, Innovation 2 (2021).

[36] Y.N. Chen, Q.Q. Zhou, Z.F. Jia, N. Cheng, S. Zhang, W.D. Chen, L. Wang, Enhancing cancer immunotherapy: nanotechnology-mediated immunotherapy overcoming immunosuppression, Acta Pharm. Sin. B 14 (9) (2024) 3834–3854.

[37] Z.C. Xiao, Y.T. Tan, Y.J. Cai, J.S. Huang, X.B. Wang, B. Li, L.T. Lin, Y. Wang, X.T. Shuai, K.S. Zhu, Nanodrug removes physical barrier to promote T-cell infiltration for enhanced cancer immunotherapy, J. Contr. Release 356 (2023) 360–372.

[38] P.L. Lu, D.X. Ruan, M.Q. Huang, M. Tian, K.S. Zhu, Z.Q. Gan, Z.C. Xiao, Harnessing the potential of hydrogels for advanced therapeutic applications: current achievements and future directions, Signal Transduct. Targeted Ther. 9 (1) (2024).

[39] S. Wang, H.L. Shen, Q.L. Mao, Q. Tao, G.T. Yuan, L.L. Zeng, Z.Y. Chen, Y.J. Zhang, L. Cheng, J.Z. Zhang, H. Dai, C.H. Hu, Y. Pan, Y.G. Li, Macrophage-mediated porous magnetic nanoparticles for multimodal imaging and postoperative photothermal therapy of gliomas, Acs Appl Mater Inter 13 (48) (2021) 56825–56837.

[40] S. Sharma, P. Ram, Capturing of magnetic nanoparticles in a fluidic channel for magnetic drug targeting, J. Nanosci. Nanotechnol. 21 (6) (2021) 3588–3595.

[41] C. Pucci, A. Degl'Innocenti, M.B. Gumus, G. Ciofani, Superparamagnetic iron oxide nanoparticles for magnetic hyperthermia: recent advancements, molecular effects, and future directions in the omics era, Biomater Sci-Uk 10 (9) (2022) 2103–2121.

[42] Q. Fan, L. Kuang, B. Wang, Y. Yin, Z. Dong, N. Tian, J. Wang, T. Yin, Y. Wang, Multiple synergistic effects of the microglia membrane-bionic nanoplatform on mediate tumor microenvironment remodeling to amplify glioblastoma immunotherapy, ACS Nano 18 (22) (2024) 14469–14486.

[43] S. Zhang, X.J. Zhang, H. Gao, X.Q. Zhang, L.D. Sun, Y.Y. Huang, J. Zhang, B.Y. Ding, Cell membrane-coated biomimetic nanoparticles in cancer treatment, Pharmaceutics 16 (4) (2024).

[44] C.F. Rodrigues, I.J. Correia, A.F. Moreira, Red blood cell membrane-camouflaged gold-core silica shell nanorods for cancer drug delivery and photothermal therapy, Int. J. Pharm. (Amst.) 655 (2024).

[45] R.H. Fang, W.W. Gao, L.F. Zhang, Targeting drugs to tumours using cell membrane-coated nanoparticles, Nat. Rev. Clin. Oncol. 20 (1) (2023) 33–48.

[46] A. Dabbagh, Z. Hedayatnasab, H. Karimian, M. Sarraf, C.H. Yeong, H.R. Madaah Hosseini, N.H. Abu Kasim, T.W. Wong, N.A. Rahman, A, Polyethylene glycol-coated porous magnetic nanoparticles for targeted delivery of chemotherapeutics under magnetic hyperthermia condition, Int. J. Hyperther. 36 (1) (2019) 104–114.

[47] H.L. Jiang, Q. Bao, T. Yang, M.Y. Yang, C.B. Mao, Precision treatment of colon cancer using doxorubicin-loaded metal-organic-framework-coated magnetic nanoparticles, ACS Appl. Mater. Interfaces 16 (37) (2024) 49003–49012.

[48] S.Y. Zang, K.X. Huang, J.X. Li, K.B. Ren, T. Li, X. He, Y. Tao, J. He, Z.Y. Dong, M. Li, Q. He, Metabolic reprogramming by dual-targeting biomimetic nanoparticles for enhanced tumor chemo-immunotherapy, Acta Biomater. 148 (2022) 181–193.

[49] C. Xiao, C.Y. Tong, J.L. Fan, Z. Wang, Q. Xie, Y. Long, P.D. You, W. Wang, B. Liu, Biomimetic nanoparticles loading with gamabutolin-indomethacin for chemo/photothermal therapy of cervical cancer and anti-inflammation, J. Contr. Release 339 (2021) 259–273.

[50] S.C. Zhang, W.B. Chen, Y.Y. Zhou, X.W. Zheng, Y. Fu, H.Y. Liu, Z. Wan, Y.L. Zhao, Intelligent nanoplatform integrating macrophage and cancer cell membrane for synergistic chemodynamic/immunotherapy/photothermal therapy of breast cancer, ACS Appl. Mater. Interfaces 15 (51) (2023) 59117–59133.

[51] J.Q. Xiong, M. Wu, J.L. Chen, Y.F. Liu, Y.R. Chen, G.L. Fan, Y.Y. Liu, J. Cheng, Z.H. Wang, S.X. Wang, Y. Liu, W. Zhang, Cancer-erythrocyte hybrid membrane-camouflaged magnetic nanoparticles with enhanced photothermal-immunotherapy for ovarian cancer, ACS Nano 15 (12) (2021) 19756–19770.

[52] W. Zhang, C.N. Gong, Z.Q. Chen, M. Li, Y.P. Li, J. Gao, Tumor microenvironment-activated cancer cell membrane-liposome hybrid nanoparticle-mediated synergistic metabolic therapy and chemotherapy for non-small cell lung cancer, J. Nanobiotechnol. 19 (1) (2021).

[53] B. Farhood, M. Najafi, K. Mortezaee, CD8+ cytotoxic T lymphocytes in cancer immunotherapy: a review, Cellular Physiology 234 (6) (2019) 8509–8521.

[54] C.W. Li, H.Y. Guo, P.S. Zhai, M. Yan, C. Liu, X.N. Wang, C.J. Shi, J. Li, T. Tong, Z.Y. Zhang, H.L. Ma, J.J. Zhang, Spatial and single-cell transcriptomics reveal a cancer-associated fibroblast subset in HNSCC that restricts infiltration and antitumor activity of CD8+ T cells, Cancer Res. 84 (2) (2024) 258–275.